



BIOPERIANT12: a mesoscale resolving coupled physics-biogeochemical model for the Southern Ocean

Nicolette Chang^{1,2}, Sarah-Anne Nicholson¹, Marcel du Plessis³, Alice D. Lebehot¹,
Thulwaneng Mashifane¹, Tumelo C. Moalusi^{1,2}, N. Precious Mongwe^{1,4}, and Pedro M.S. Monteiro^{1,2,5}

¹Southern Ocean Carbon-Climate Observatory, CSIR, Cape Town, South Africa

²Global Change Institute, University of the Witwatersrand, Johannesburg, South Africa

³Department of Marine Science, University of Gothenburg, Sweden

⁴National Institute for Theoretical and Computational Sciences (NITheCS), South Africa

⁵School for Climate Studies, Stellenbosch University, Stellenbosch, South Africa

Correspondence: Nicolette Chang (nchang@csir.co.za)

Abstract. We present BIOPERIANT12, a regional model configuration of the Southern Ocean (SO) at a mesoscale-resolving 1/12°. This is a stable, ocean–ice–biogeochemical configuration derived from the Nucleus for European Modelling of the Ocean (NEMO) modelling platform. It is specifically designed to investigate questions related to the mean state, seasonal cycle variability and mesoscale processes in the mixed layer and within the upper ocean (<1000 m). In particular, the focus is on understanding processes behind carbon and heat exchange, systematic errors in biogeochemistry and assumptions underlying the parameters chosen to represent these SO processes. The dynamics of the ocean model play a large role in driving ocean biogeochemistry and we show that over the chosen period of analysis 2000–2009 that the simulated dynamics in the upper ocean provide a stable mean state, as compared to observation-based datasets (themselves subject to biases such as sparsity of data, cloud cover, etc.), and through which the characteristics of variability can be described. Using ocean biomes to delineate the major regions of the SO, the model demonstrates a useful representation of ocean biogeochemistry and partial pressure of carbon dioxide (pCO₂). In addition to a reasonable model mean state performance, through model–data metrics BIOPERIANT12 highlights several pathways for improving Southern Ocean model simulations such as the representation of temporal variability and the overestimation of biological biomass.



1 Introduction

15 The Southern Ocean (SO) is an essential sink of carbon dioxide (CO₂) and heat, responsible for nearly 40 % of the global ocean annual mean CO₂ uptake and 75 % of the excess heat globally (Frölicher et al., 2015; Gruber et al., 2023). Since the 2000s, this sparsely observed region has been increasingly sampled (Williams et al., 2018; Meredith et al., 2013; Swart et al., 2012). These efforts, conducted at increasing temporal and spatial resolutions, have exposed the challenge of accurately representing CO₂ heat fluxes of the SO within ocean models and by extension, earth system models (ESMs) from which
20 projections are made (Rintoul, 2018), despite being weakly constrained and seasonally biased themselves. The seasonal cycle is arguably the dominant mode of variability in physical-biogeochemical properties of the SO (Lenton et al., 2013; Thomalla et al., 2011; Mongwe et al., 2018; Gregor et al., 2019; Rodgers et al., 2023), yet the state-of-the-art, particularly the ocean components of ESMs (Chassignet et al., 2020; Treguier et al., 2023), display inadequate representation of these scales. Large model biases in ESMs are seen in the wide, inter-model spread of the contributing models in the previous generations of
25 Climate Model Intercomparison Project (CMIP). This is particularly evident in the pronounced inability to reproduce similar seasonal cycles of air-sea CO₂ flux (FCO₂) (Anav et al., 2013; Lenton et al., 2013; Kessler and Tjiputra, 2016; Mongwe et al., 2016, 2018), sea-ice extent and trends (Meijers, 2014; Beadling et al., 2020), mixed layer depth (MLD) (Sallée et al., 2013; Treguier et al., 2023), water mass properties (Downes et al., 2015; Beadling et al., 2020), dissolved iron (Tagliabue et al., 2016) and phytoplankton phenology (Thomalla et al., 2011, 2023; Hague and Vichi, 2018). Key to reproducing the heat and CO₂
30 fluxes in the SO, are the representation of the dynamics in models, particularly the ubiquity of mesoscale eddies due to the strong baroclinically induced instabilities of the Antarctic Circumpolar Current (ACC) and associated strong mesoscale kinetic energy (Daniault and Ménard, 1985; Smith et al., 2023). Mesoscale dynamics explain a substantial portion of the annual and seasonal variance in mixed-layer depths (Whitt et al., 2019; Gaube et al., 2019), and therefore influence global circulation by impacting water mass transformation and influencing the SO overturning circulation through eddy compensation and sensitivity
35 of wind (Abernathey et al., 2016; Munday et al., 2014). Mesoscale and also submesoscale dynamics, through enhancements in advection and mixing, consequently influence the local biogeochemistry (BGC) and thus carbon exchange, such as by altering the supply of limiting nutrients to the euphotic layer (Frenger et al., 2015; Nicholson et al., 2019; Uchida et al., 2019) and available light via "eddy slumping" induced stratification during spring (Lévy et al., 1998, 1999; Marshall et al., 2002; Lévy et al., 2010; Mahadevan et al., 2012). Simulations with coupled physics-BGC in global (Rohr et al., 2020) and regional
40 ocean models (Song et al., 2018; Uchida et al., 2019, 2020) show the variability in both biological and physical mechanisms due to eddies influence the biological response in the SO with implications both spatially and temporally, such as in the characteristics of the seasonal cycles of both physical and BGC processes. Computational cost is still a limiting factor in the design of both projection and process models; while computational power (and horizontal model resolution) has increased from CMIP5 (resolutions of 1° or coarser and relied on suitable parameterisations), CMIP6 only has resolutions of up to 0.25° which
45 allows some explicit representation of the ocean (Hewitt et al., 2020; Haarsma et al., 2016), these do not include the mesoscale. Model configurations with BGC, therefore, compromise in spatial/temporal resolution or run duration and model complexity. For example, the MOMSO configuration (Modular Ocean Model Southern Ocean, Dietze et al., 2020) is eddy-resolving in the



SO (11 km resolution at 40° S) but has a reduced BGC model (BLING) consisting of 4 BGC tracers and a carbon module for climatologically forced, multi-decadal experiments. SO iron supply experiments by Uchida et al. (2019), on the other hand, use a full BGC model with phytoplankton and zooplankton functional groups, but an idealised ocean of 20 km resolution, flat-bottomed, re-entrant channel. BGC data assimilation for SO flux experiments in B-SOSE (Biogeochemical Southern Ocean State Estimate) uses model resolution (1/3°, Verdy and Mazloff, 2017, and 1/6°, <http://sose.ucsd.edu/>) and run duration which relies on periods of sufficient observations. These configuration compromises contribute to uncertainties in carbon and heat exchange, particularly for climate-scale questions using long-running models (Hewitt et al., 2020; Beadling et al., 2020). The importance of model resolution is apparent through, firstly, the representation of ocean dynamics that distribute BGC tracers in the model and are the major driver of the BGC differences of simulations with observations and between simulations in ESMs, for example, mesoscale modulations of the MLD affect light and iron supply to surface influencing phytoplankton growth and thus the biological carbon pump (Song et al., 2018). Secondly, resolution affects the evolution of the tracers themselves, (Séférian et al., 2013) discuss errors in the BGC fields which may propagate spatially and amplify during model evolution in low resolution simulations, particularly the pools of nutrients and iron which supply the surface, although this matters more for simulations of hundreds of years versus the short model duration of BIOPERIANT12. To understand the heat and carbon biases in SO models, we focus on understanding the biophysical dynamics in the ocean surface mixed-layer, the boundary across which atmosphere-ocean exchange occurs. In this paper, we present a regional, circumpolar, mesoscale-resolving (1/12°), contemporary ocean-ice-biogeochemical, NEMO-PISCES model configuration, BIOPERIANT12. This configuration has a laterally unconstrained ACC with resolved eddies, and a prescribed atmosphere to evolve the SO over a limited duration (20 years). We describe the model design in Section 2. In Section 3, we assess the configuration looking at model stability and, through a comparison against observations, suitability to serve as an experimental platform and for downscaling, submesoscale experiments and sensitivity studies coinciding with in situ experiments (Swart et al., 2012; du Plessis et al., 2022; Djeutchouang et al., 2022; Smith et al., 2023).

2 BIOPERIANT12 model configuration

BIOPERIANT12 (full configuration name: BIOPERIANT12-CNCLNG01) is a regional, mesoscale-resolving configuration for simulating the ocean, ice, and biogeochemistry of the circumpolar SO for contemporary conditions. NEMO-PISCES version 3.4 (Gurvan et al., 2019) with specifications by the DRAKKAR consortium (Barnier et al., 2014) was used. This consists of an ocean-ice component provided by the OPA (Océan Parallélisé) model and Louvain-la-Neuve Sea Ice Model (LIM2) and biogeochemical components by PISCES (Aumont and Bopp, 2006; updated version Aumont et al., 2015). Although more recent versions were available at production, this model version was used to be consistent with configuration development, starting with a hierarchy of tests of increasing resolution on which model parameters were tested. This model run was configured from two other previous model runs from the DRAKKAR Group and will be referred to several times below: ORCA12-MAL101, a global physics only run (Barnier et al., 2014; Lecointre et al., 2011) and BIOPERIANT05-GAA95b, an eddy-permitting SO

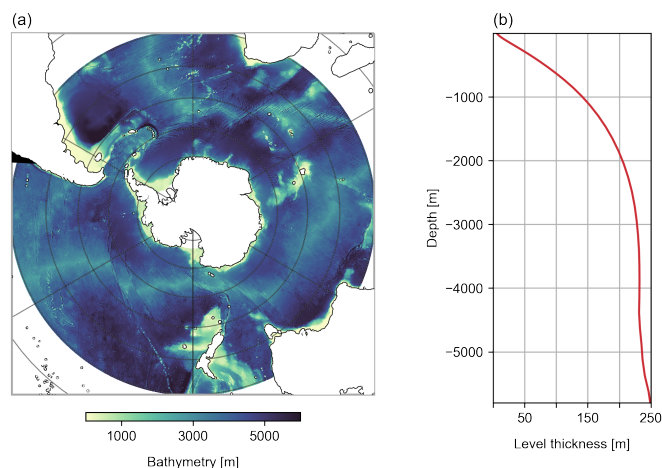


Figure 1. BIOPERIANT12 grid configuration (a) domain showing model bathymetry and (b) vertical grid thickness versus depth.

80 configuration including biogeochemistry (Albert, A. pers. comm, MEOM-DRAKKAR group), an updated model of Dufour
et al. (2013) from which we derived our designation of BIOPERIANT12.

2.1 Domain and grid

The model grid and bathymetry for the Southern Ocean south of 30° S (Fig. 1a) is a subset of the global tripolar ORCA12
grid with 46 vertical levels built from the ETOPO2 dataset combined with the GEBCO one minute grid. The horizontal grid, at
85 1/12° resolution (~8 km at 30° S, 4.6 km at 60° S), can be considered eddy-resolving. The vertical grid of BIOPERIANT12
consists of 46 z-coordinate levels with partial bottom steps. For the surface ocean mixed layer fluxes and biogeochemistry, there
are 15/18 levels in the upper 200/400 m, with vertical resolution ranging from 6–40 m. Below this, grid thickness increases:
~200 m at 2000 m depth ($z = 29$) and finally 250 m at the bottom (Fig. 1b).

2.2 Initial conditions

90 To obtain a representative and stable surface ocean state, BIOPERIANT12 is initialised from rest and for tracers from respective
climatological products. For the ocean, Levitus temperature and salinity climatology (Locarnini et al., 2010) were used. Sea ice
initial conditions are from the January ice climatology for 1998–2007 from ORCA12-MAL101, when sea ice is at a minimum
in the seasonal cycle and thereafter freely evolves with the LIM2 model. Biogeochemical tracers were initialised from coarse-
resolution climatologies: dissolved inorganic carbon (DIC), total alkalinity (TA) from the GLODAP annual climatology (Key
95 et al., 2004); nitrate (NO_3), phosphate (PO_4), silicate (Si) and oxygen (O_2) from the January monthly WOA09 climatology
(Garcia et al., 2013, 2010); dissolved organic carbon and iron were consistent with the BIOPERIANT05-GAA95b initialisation
90 from an ORCA05 run. The other tracers were initialised with constant values set in PISCES.



2.3 Boundary Conditions

BIOPERIANT12 has one open lateral boundary in the north. Boundary conditions for the dynamics were derived from an ORCA12–MAL101 from the available 5 day averages for 1989–2009. While the BIOPERIANT12 dynamical open boundary conditions are of a comparative $1/12^\circ$ resolution, biogeochemical boundary conditions were not available at this high resolution at the time of preprocessing; we therefore obtained them from the coarser $1/2^\circ$ BIOPERIANT05-GAA95b. A climatological “normal year” boundary forcing consisting of 5 day averages for the period 1995–2009 was calculated and used as opposed to the interannual dataset due to reported biases in certain biogeochemical tracers (Mongwe et al., 2016). For the lateral boundary of the coastlines partial free slip is prescribed. Surface atmospheric forcing data are from ERA-interim (Dee et al., 2011) using the CORE bulk formulation. Wind components are supplied at 3 hourly intervals using the absolute wind formulation thus neglecting effects of the surface ocean current on the wind. Sea surface restoring of salinity to Levitus monthly climatology is applied. Restoring for Antarctic Bottom Water is applied to counteract the drift in ACC transport due to the representation of deep waters in the DRAKKAR models (Dufour et al., 2012).

2.4 Model evolution

The model is run for the duration 1989 to 2009, the same period for which the ORCA12 boundary conditions were available. The model integration was carried out with a baroclinic time step of 360 s. Within the first 5 years of initialisation surface ocean dynamics reach statistical equilibrium and transport through the Drake Passage stabilises, years 1989 to 1994 are therefore designated as spin-up (Fig. S1, S2). Thereafter the model is run to 2009 with output saved as 5 day averages and the final 10 years (2000–2009) were analysed. At depths below 400 m, temperature shows a significant drift from 2002, while the aim is to simulate surface ocean processes, this must be noted when using the model output.

2.5 Model Numerics

Ocean tracers (temperature and salinity) advection is implemented with the TVD scheme, while passive PISCES tracers are advected using the MUSCL advection scheme. Lateral diffusion of both ocean and passive tracers is achieved with a laplacian operator along isonetural surfaces. Lateral advection of momentum uses a leapfrog scheme; momentum diffusion uses the bilaplacian operator along geopotential surfaces. Vertical mixing in the model uses the turbulent kinetic energy (TKE) closure scheme. For subgrid-scale mixing in the background, vertical eddy viscosity and diffusivity coefficients are set to $1.2 \times 10^{-4} \text{ m}^2 \text{ s}^{-1}$ and $1.2 \times 10^{-5} \text{ m}^2 \text{ s}^{-1}$. At the bottom, a diffusive bottom boundary layer scheme is used as well as the advective bottom boundary layer scheme for the case of dense water overlying less dense water at the bottom (Gurvan et al., 2019). The bottom boundary is set with nonlinear bottom friction.

2.6 Computational Requirements

Development of BIOPERIANT12 started after the introduction of the Lengau cluster of NICIS-CHPC (Centre for High Performance Computing) in late 2016, which comprises of approximately 32 832 Intel XEON CPU cores when fully operational



and is a shared HPC resource of the South African research community. The final iteration, this reference simulation, was run
130 in 2020. Due to South African electricity restrictions, compute capacity, resource allocation and system stability decrease, to
compensate for this, we chose to use more storage space to create and save restart files more frequently. Even with the NEMO
land elimination algorithm eliminating 19 % of the non-ocean subdomains, 3240 CPUs were chosen to balance model scaling
and wall clock time for running and saving ocean, ice and BGC 5 day outputs as well as restart files.

3 Model Evaluation

135 We evaluate BIOPERIANT12 physical and biogeochemical fields by comparing key metrics of the upper-ocean for the last 10
years of the experiment, 2000–2009, against observations (OBS), for which temporal and spatial coverage improves within the
2000s. Observational datasets are provided inline and summarised in Table 1. We note that many datasets are low resolution,
gridded products, which is only applicable in evaluating the large-scale mean-state. We check that the model reproduces
annual and seasonal mean states as an initial comparison and then follow this with the characteristics of temporal variability.
140 In Section 3.1, we evaluate the model physical ocean and ice properties as an indication of model stability and the general
circulation affecting the BGC tracers, guided by the metrics proposed by Russell et al. (2018) for the evaluation of the SO
in coupled climate models and ESMs. As a summary, preceding further evaluation of the BGC output, we present biomes
and summarisw the model output compared to that of observations (Section 3.2). In Section 3.3, we present modelled carbon.
Finally, biogeochemical and biological properties are further analysed in Section 3.4.

145 3.1 Key physical ocean metrics in the Southern Ocean

3.1.1 Transport through Drake Passage

Transport of the ACC through the Drake Passage at 69° W in BIOPERIANT12 is stable after spin-up (Fig. S2), with annual
mean transport through the Drake Passage from 2000–2009 at 145.25 ± 5.66 Sv. The value is comparable with observations
as summarised in Table 2, such as the generally accepted observational estimate of 134 ± 11.2 Sv by Whitworth and Peterson
150 (1985); although estimates of transport taken after 2007 yield values higher than this, e.g 173.3 ± 10.7 Sv (Donohue et al., 2016),
attributed to higher resolution observations and is used as the observational benchmark for the model analysis of CMIP3 to
CMIP6 models by Beadling et al. (2020). It also compares well to its similar SO regional model “predecessors” PERIANT05
and PERIANT025 of (0.5° and 0.25° resolution, respectively), with respective mean transports of 149.2 Sv and 143.2 Sv
(Dufour et al., 2012), as well as the multi-model mean of 155 ± 51 Sv for CMIP5 global models of mostly 1° resolution
155 (Meijers, 2014) and similar to eddy-resolving Ocean Model Intercomparison Project phase 2 (OMIP-2) models that fall within
the chosen observation range of 134–173 Sv (Chassignet et al., 2020).



Table 1. Summary of observational datasets used for model evaluation

Variable	Temporal resolution and coverage	Horizontal resolution	Dataset and reference URL
Currents u, v	2000–2009	0.25°	AVISO altimetry (The Ssalto/Duacs altimeter products were produced and distributed by the Copernicus Marine and Environment Monitoring Service, CMEMS, http://www.marine.copernicus.eu)
Temperature, Salinity	Monthly climatology	0.25°	WOA2013 (Locarnini et al., 2010)
Polar Front position	Weekly 2002–2009	0.25°	Satellite (Freeman and Lovenduski, 2016)
MLD gridded	Monthly climatology	1°	Argo profiles (Holte et al., 2017)
T/S profiles	2002–2009		Argo profiles (Holte et al., 2017)
Sea ice concentration	2000–2009	0.25°	NOAA/NSIDC (Meier et al., 2017; Peng et al., 2013)
Mean biomes	Mean over 1998–2010	1°	Biome dataset (Fay and McKinley, 2014)
FCO ₂ , pCO ₂	Monthly means	1°	CSIR-ML6 multi-platform machine-learning product (Gregor et al., 2019)
DIC, TA	Annual mean centred 2002	1°	GLODAPv2 (Olsen et al., 2016; Lauvset et al., 2016)
Dissolved iron	Binned into months	1° bins	Dissolved iron in situ profiles (Tagliabue et al., 2014)
NO ₃ , PO ₄ , Si	Monthly climatology	1°	WOA13 (Garcia et al., 2010)
Dissolved oxygen	Monthly climatology	1°	WOA13 (Garcia et al., 2013)
Chlorophyll-a	Weekly 2000–2009	9 km	OC-CCI-v6 mixed satellite in situ chlorophyll-a (Sathyendranath et al., 2019)

3.1.2 Eddy Kinetic Energy (EKE)

Figure 2 shows the climatological annual mean surface EKE for 2000–2009 for the model compared to the EKE derived from AVISO 1/4° gridded altimetry dataset. The distribution of EKE in the model is in general agreement with observations, regions of high EKE such as those associated with western boundary currents and downstream of topography are represented in the model. Zonally averaged EKE bands are comparable to SO models by Munday et al. (2021, Fig. 7a), although BIOPERIANT12 shows slightly higher EKE than their models, except for the WBC regions. BIOPERIANT12 appears to overestimate EKE except between 36 and 43° S (Fig. 2a) particularly from the Agulhas Current region (Fig. S2) as seen in the meridionally averaged EKE between 15–45° E (Fig. S3). Models at similar resolutions are able to represent the distribution patterns of



Table 2. BIOPERIANT12 Drake Passage transport vs selected estimates from literature

Transport [Sv]	Source	Reference
145.25 ±5.66	BIOPERIANT12	
134 ±11.2	Observations	Whitworth and Peterson (1985)
173.3 ±10.7	Observations after 2007	Donohue et al. (2016)
149.2	Model 0.5° resolution (PERIANT05)	Dufour et al. (2012)
143.2	Model 0.25° resolution (PERIANT025)	Dufour et al. (2012)
155 ±51	CMIP5 multi-model mean (1° resolution)	Meijers (2014)
134–173	OMIP-2 models eddy-resolving	Chassignet et al. (2020)

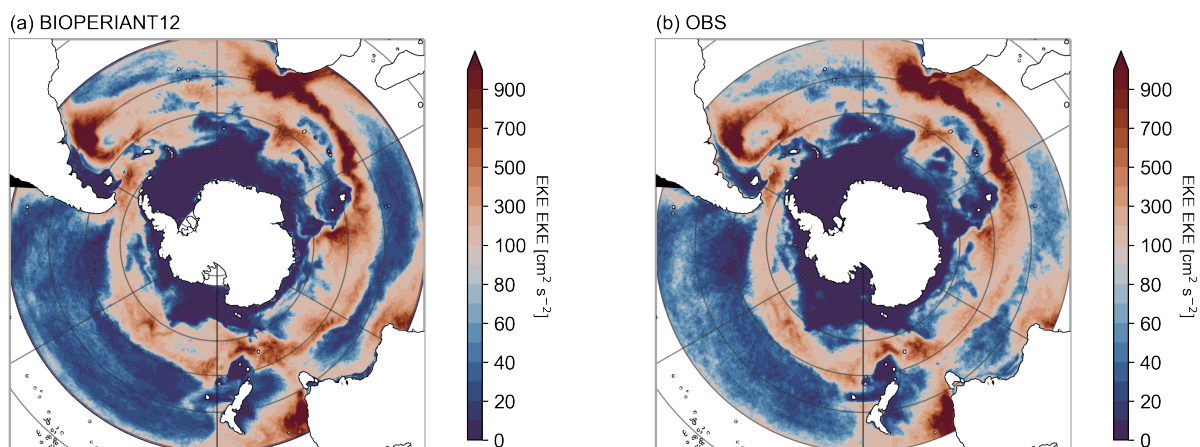


Figure 2. Annual mean surface EKE for years 2000–2009 for (a) BIOPERIANT12 model and (b) the AVISO 1/4° dataset.

165 EKE (e.g. ORCA12, (Rieck et al., 2015; Patara et al., 2016)), although magnitudes may differ. Most OMIP-2 ocean models (at
 ~1/10°) underestimate EKE with some contribution from temporal averaging (Chassignet et al., 2020), regional effects may
 also contribute: high EKE regions are eddy-rich but their spatial coverage in OMIP-2 models are smaller than observations
 (AVISO) while eddy-poor regions have greater spatial coverage. Regional model MOMSO (Dietze et al., 2020), on the other
 hand, overestimates EKE, which is attributed to the higher model than observational dataset resolution, degrading model spatial
 170 resolution obtains more comparable magnitudes. With consideration to factors such as regional differences, such as in the effect
 of winds (Patara et al., 2016) and applying the absolute wind formula which neglects the effect of current-wind interactions
 and reduces eddy energy (Renault et al., 2016; Munday et al., 2021), BIOPERIANT12 EKE describes a surface SO with
 reasonable mesoscale eddy representation with which physical dynamics towards model improvement and BGC questions can
 be addressed.



175 3.1.3 Frontal structure

The SO fronts help describe the larger ACC structure, with their steep horizontal gradients and associated strong vertical motion, they demarcate regions of consistent water and nutrient properties, as well as regions of CO₂ in- and out-gassing: CO₂ in-gassing north of the Polar Front (PF) and out-gassing between the PF southwards to the marginal ice zone (Mongwe et al., 2018). Latitudinal variations in the frontal positions will thus reflect as local changes which affect heat and carbon
180 fluxes and are therefore used as a SO evaluation metric by Russell et al. (2018), the positions of the SubAntarctic Front (SAF) and PF are chosen out of all the SO fronts, as representing the northern boundary and the central ACC, respectively. Their method uses a simplified subsurface temperature criteria consistent with (Orsi et al., 1995) which allows easy inter-model and model-observation comparisons: the SAF is defined by the 4 °C isotherm at 400 m and the PF by the 2 °C isotherm in the upper 200 m. In Figure 3, we present the annual-mean position and standard deviation of the SAF and PF for BIOPERIANT12
185 interannual monthly-means, compared to those derived from WOA13 temperature (climatological months), the satellite-derived PF of Freeman and Lovenduski (2016), and Orsi et al. (1995), as used by Russell et al. (2018). In general, spatial meridional variabilities in the model frontal positions are consistent with the observation-derived fronts, but with a south bias by up to 3° in latitude, showing "pinching" of the fronts from topography such as Drake Passage, Campbell Plateau (170° E) and the Southwest (30° E) and Southeast (80° E) Indian Ridge, followed by diverging of the SAF and PF downstream. However, the
190 difference in the model PF in the Indian Ocean stands out, highlighting the nature of averaging or the temporal under sampling of data. At the Kerguelen Plateau (~75° E), the model follows either the northern or southern branch but the mean PF reflects the southern path (see Fig. S4) accompanied by very high standard deviation in contrast to data that show the mean path favours the northern branch over the northern plateau (Dong et al., 2006; Wang et al., 2016). As with the examples provided by Russell et al. (2018), the chosen models do not completely or consistently capture similar patterns to the observations, reflecting their
195 individual model biases as well as their coarser resolution (CMIP5 models at ~100 km). As shown in model EKE in Fig. 2, the mean mesoscale dynamics of the SO are captured by BIOPERIANT12, this includes the complex frontal dynamics described in observational studies such as branching, jets and front-eddy interaction (Freeman and Lovenduski, 2016; Chapman, 2017) which ultimately affects the calculated frontal positions particularly, a temperature-derived definition. The high variability in frontal dynamics of the mesoscale-resolving BIOPERIANT12, leads to model-observation differences, especially for regions
200 such as the Kerguelen Plateau which is dominated by eddies as opposed to the meandering of the core jets (Shao et al., 2015); additionally, we expect a corresponding improved exchange of water and biogeochemical properties (Rosso et al., 2020). This complicates this metric for model-observation comparison but frontal position is still useful to delineate model regions for analysis.

3.1.4 Mixed Layer Depth

205 To evaluate the MLD of BIOPERIANT12, we chose in situ measurements given by the Argo floats database as our observational reference (Table 1). MLD from both sources were calculated from temperature and salinity values and using the de Boyer Montégut et al. (2004) density threshold of 0.03 kg m⁻³ from a reference depth of 10 m, a method that has been shown to

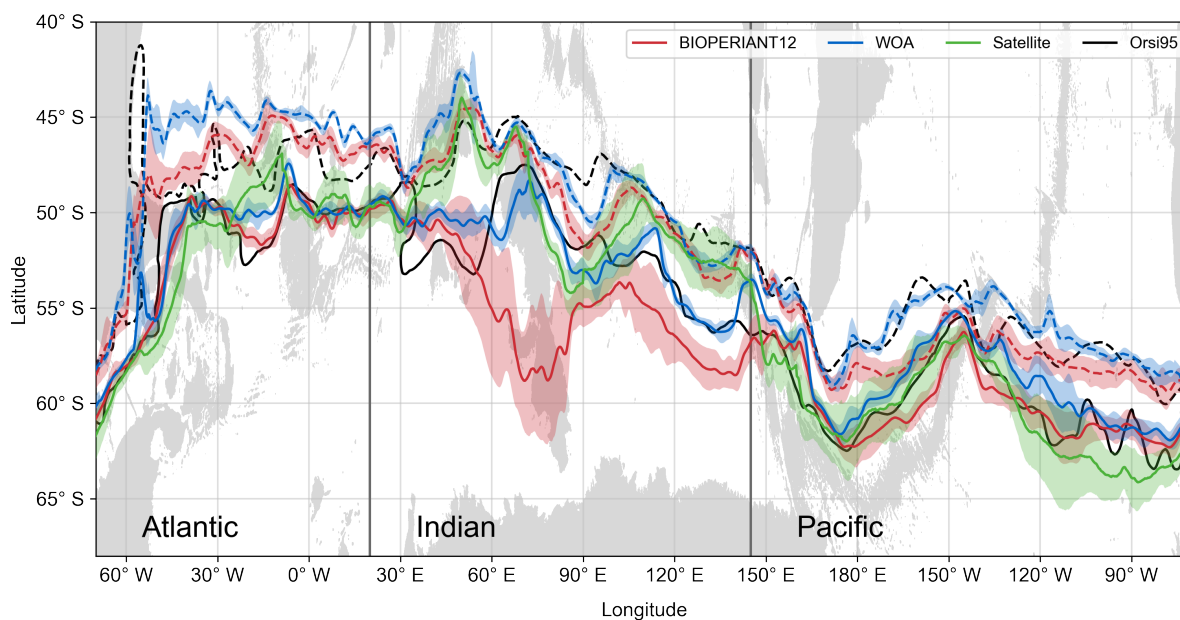


Figure 3. Annual mean latitudinal position of the SubAntarctic Front (dashed line) and Polar Front (solid line) in BIOPERIANT12 (2000–2009) compared to WOA13 and satellite Polar Front (2002–2009) from Freeman and Lovenduski (2016) and Orsi et al. (1995). Colour shaded regions are the standard deviation of the front using monthly-mean temperatures. Grey shaded regions indicate the land mask and bathymetry shallower than 3000 m (lighter grey).

be robust for Southern Ocean profiles (Dong et al., 2008; Treguier et al., 2023). While the Argo platform presents spatial and temporal gaps in their coverage (Fig. S5), the temperature and salinity profiles collected by the floats ultimately captures
210 the real-world variability and mixing features, in opposition to reanalysis products which introduce an unknown source of uncertainty depending on their reanalysis model. Model MLD was then sampled according to the Argo observational coverage. MLD observations were binned into a $1^\circ \times 1^\circ$ regular grid and averaged to monthly intervals across the period 2001–2009. This was also done for model MLD which was then further subsampled to the same locations and months as observations. The seasonal-spatial patterns and amplitude are shown in Fig. 4.

215 Overall, the spatial distribution of the observational and BIOPERIANT12 MLDs agree well, for both the minimum and maximum MLD months, January and September, respectively (Fig. 4a–b, d–e). A comparison of the magnitude of the summer MLD (Fig. 4c) shows within the ACC, the BIOPERIANT12 MLD is too deep by around 50 m while it is too shallow by around 50 m in the north of the SAF. For winter MLDs, BIOPERIANT12 generates deeper MLDs relative to the observational estimates (by about 100 m; Fig. 4f) in the Pacific sector of the SO. Despite the magnitude difference, BIOPERIANT12 captures
220 the deep winter MLDs (exceeding 400 m) confined to the Pacific and Indian sectors showing that the model is responding to atmospheric forcing and forming deep waters in the expected regions. An important component of the MLD in the SO is the seasonal cycle (Fig. 4g). The winter deepening and summer shoaling of the simulated MLD agrees well with the seasonal

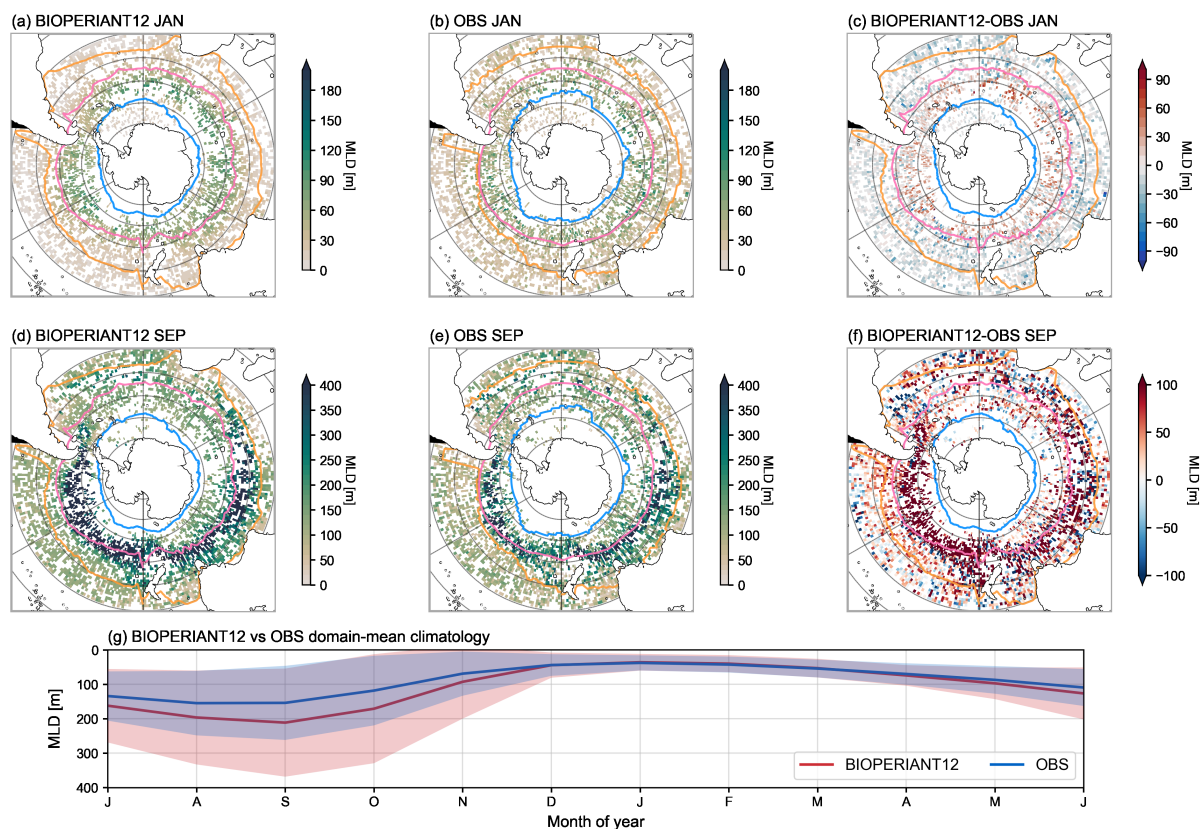


Figure 4. Seasonal comparisons of MLD from (a, d) BIOPERIANT12 averaged monthly and co-located to monthly averaged Argo MLDs in a $1^\circ \times 1^\circ$ regular grid, (b, e) Argo float observations, and (c, f) model–observation difference, for January and September climatologies respectively. Maps are overlaid with the northern climatological biome borders corresponding to model/data SO biomes. (g) Climatological seasonal cycle of monthly MLD domain-averaged over the entire SO.

225 cycle of the observations, with a monthly climatology Pearson correlation of $r = 0.97$. The shallow limit of the simulated climatological MLD follows the observations well during DJFM, however the deep MLD limit departs from the observations around April, where standard deviations of the monthly mean MLDs show the BIOPERIANT12 MLD extending to over 100 m deeper in September (MLD maximum) than what the observations show. Treguier et al. (2023) showed that in OMIP models ranging from 1° down to $1/16^\circ$ horizontal resolution, MLD is hard to constrain and increasing model resolution to include the mesoscale does not consistently improve MLD depth in the SO. Nevertheless, the seasonal cycle and variability of the BIOPERIANT12 MLD agrees well with the observations, despite over-deepening during winter.



230 3.1.5 Ocean Heat Content (OHC) and Temperature

BIOPERIANT12 temperature and OHC for the upper 400 m appear to compare well in seasonal distribution (Fig. S6). While no surface temperature correction has been applied to the model, it is relatively stable over the last 10 years of the model but model–data climatological differences between BIOPERIANT12 and WOA13 temperature and OHC show spatial variations in the mesoscale model fields (Fig. S7a, c). OHC in the model has a warm bias (domain mean around $13 \times 10^9 \text{ J m}^{-2}$, Fig. S7e), although SST shows a cool bias (Fig. S7b, d). While SO surface temperatures in models generally show warm biases (Beadling et al., 2020) and the opposite is shown for BIOPERIANT12 SST (Fig. 7f, domain-mean SST solid line), the deeper, domain-mean temperatures at 200 and 400 m are warmer than observations (Fig. S7f, dotted, and dashed lines) despite the low resolution, area-weighting of the dataset. The model–data differences are consistent over the run duration, the model is initialised with climatology and after spin-up shows no significant drift (Fig. S7g), the resultant stable upper ocean structure over the model analysis period suggests that the dynamics are also stable, possibly from increased mesoscale dynamics of the model which also influenced frontal definition above. Thus, we disregard the creation and influence of spurious features in the simulation that may propagate while altering the physical and biogeochemical fluxes, and any biogeochemical biases can be considered systematic or from model choices.

3.1.6 Sea ice

245 Sea ice plays an important role in setting the seasonal freshwater flux in the SO. Melting in the spring/summer and growth in autumn/winter sets the surface ocean salinity and thus has direct consequences for vertical and horizontal stratification dynamics (Giddy et al., 2021, 2023) and large-scale water mass transformation (Abernathey et al., 2016). For the model comparison, National Sea Ice Data Centre (NSIDC) sea ice observations mean monthly data for the period 2000–2009 were used (Table 1). Data shows sea ice grows northward from the Antarctic continent in the winter months, peaking with maximum extent in September and then melts towards the Antarctic continent to reach a minimum ice extent in February (Fig. 5). The spatial comparison for minimum/maximum climatological months (Fig. 5a, b) shows model maximum extent is comparable spatially to data but overestimates the sea ice growth by 1–2 million km^2 , around 10 % of the winter sea ice maximum (Fig. 5c, d). Data shows minimum sea ice extent in February, while in the model minimum occurs over February and March with similar values. The timing of sea ice growth and melt by BIOPERIANT12 relative to the observations (Fig. 5c, d) indicates that the model responds well to seasonal heat fluxes with minimum and maximum extent agreeing with the observations, particularly in the winter. Although the model does not melt sufficiently in December (~ 2 million km^2 relative to ~ 5 million km^2 from the observation), it compensates for this by not melting the remainder of the necessary sea ice in February (~ 5 million km^2 relative to ~ 2 million km^2 from the observations) before both the model and observations show sea ice growth from March (Fig. 5d; S8b). Overall, the sea ice in BIOPERIANT12 provides a stable temporal view of the seasonal cycle, with more interannual variability seen in the summer (Fig. S8b).

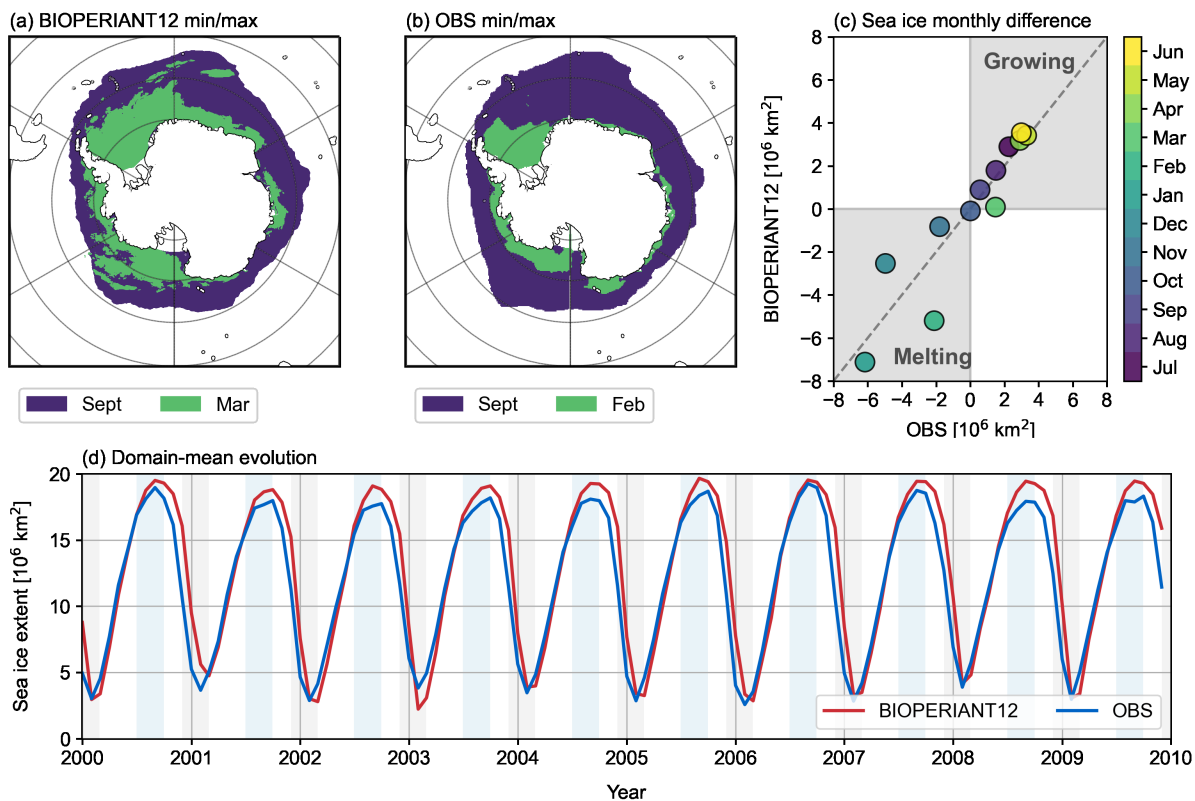


Figure 5. Climatological-mean sea ice extent of the maximum (blue) and minimum (green) months for (a) BIOPERIANT12 and (b) NSIDC observations. (c) Climatological monthly-mean sea ice extent difference indicating growth and melt for the BIOPERIANT12 simulation vs NSIDC observations. (d) Timeseries of monthly-mean sea ice extent from BIOPERIANT12 model (red) and NSIDC observations (blue).

3.2 Biomes

3.2.1 Biome definition

To evaluate the biogeochemical and carbon fields, we chose to use the biome classification method (Fay and McKinley, 2014), over static geographic definitions or that from ocean physics (e.g. by fronts, a dynamical field), thus combining both large
 265 scale physical and biogeochemical characteristics to delineate regions of biogeochemical similarity (biomes). BIOPERIANT12 mean biomes (Fig. 6a) were calculated using the model's climatological sea surface temperature (SST), Chlorophyll-a, MLD and sea ice fraction fields. The Fay and McKinley (2014) biome product based on 1998–2010 climatology (Fig. 6b) will be used to aggregate observational data. We thus compare similar, biophysically consistent SO regions between the simulated variables and the observations for the following biomes: the ice biome (SO-ICE), the subpolar seasonally stratified biome (SO-
 270 SPSS), and the subtropical seasonally stratified biome (SO-STSS). Other southern hemisphere biomes were not considered, BIOPERIANT12 does not fully capture the subtropical mean state (SP-STPS, SA-STPS and IND-STPS) which results in about



60 % less area coverage than the corresponding observed biomes and slightly overestimates the SO-STSS, SO-SPSS (Fig. 6c). Thus, the biome criteria may suggest some of the model–observation gaps (Fig. S9, S10) as well as address the effect of mesoscale features that are resolved in the higher resolution model compared to the gridded data used in the Fay and McKinley (2014) biome product and is discussed in the Supplementary.

3.2.2 Biome characteristics

To characterise the seasonal cycle of the model, we present the surface mean seasonal cycle of selected variables for each SO biome (Fig. 7) and biome-mean metrics in Table 3 (Table S1 for 200 m). To contextualise the upper water column of the biome, particularly the influence on surface pCO₂ in highly seasonally stratified areas, vertical profiles per biome are provided in Fig. S11. In Table 3, the biome-mean seasonal cycle for model and observations (as shown in Fig. 7) are given by mean and amplitude (difference between the minimum and maximum values). To compare the model’s seasonal cycle and that of the observational data, we used: the correlation coefficient between model and data (R), ratio of standard deviation (RSD), model Reliability Index (RI), and Seasonal Cycle Reproducibility (SCR). The RSD shows how the model variability compares to that expected by the observed dataset, a value of one suggests they compare well. We highlight certain regions in the model which are inconsistent with data by regions where the model variability exceeded that of observations by 50 % and where model variability was less than 50 % of the expected variability. The model RI or geometric root-mean square error (Leggett and Williams, 1981; Doney et al., 2009), gives the model–data bias that is normalised to the data and used for data that are log-normal distributed; a value of one indicates perfect agreement, while two indicates that the error is of similar magnitude to the data. The metric SCR is defined in Thomalla et al. (2011) as the correlation coefficient of the interannual varying time series at its full temporal resolution against its climatological seasonal cycle (Fig. S12 for further explanation), i.e. how well the mean climatological seasonal cycle represents the evolution of a property over each year. SCR higher than 0.85 defines a region of high SCR (e.g. high seasonality), 0.65 to 0.85 medium SCR and below 0.65, low SCR (e.g. low seasonality). The SCR for observational products were only calculated if they had an adequate temporal resolution (higher than monthly).

High resolution observations show that the seasonal response of BGC to physical forcing in the SO are regionally dependent. Model–data agreement results from a combination of factors: the available/applied observational dataset (listed in Table 1); which carries uncertainty due to poor sampling/spatiotemporal resolution and are oftentimes interpolated into gridded products and only available as climatologies; the application of biome definitions over regions of high variability (EKE) which is not used for biome definition but is shown to improve pCO₂ bias and root mean square error (Gregor et al., 2019); and the effect of area-weighted, domain averaging over large regions/biomes. In contrast to regions dominated by intraseasonal variability where observations are difficult to constrain (Monteiro et al., 2015), the seasonal cycle metrics are expected to agree with the data in regions where the response of the model is also seasonally driven with high SCR.

In general, the metrics (Table 3, Fig. 7) show the model seasonal cycle agrees with that of the data, for example, the temperature seasonal cycle per biome is well represented, however, a reasonable comparison with the data is expected since temperature is a criterion used in the biome definition. We, therefore, focus on the model-observation disagreements which highlight regions of interest. For the dynamics, there is a poor correlation of salinity in the SO-STSS region (R=0.62), this

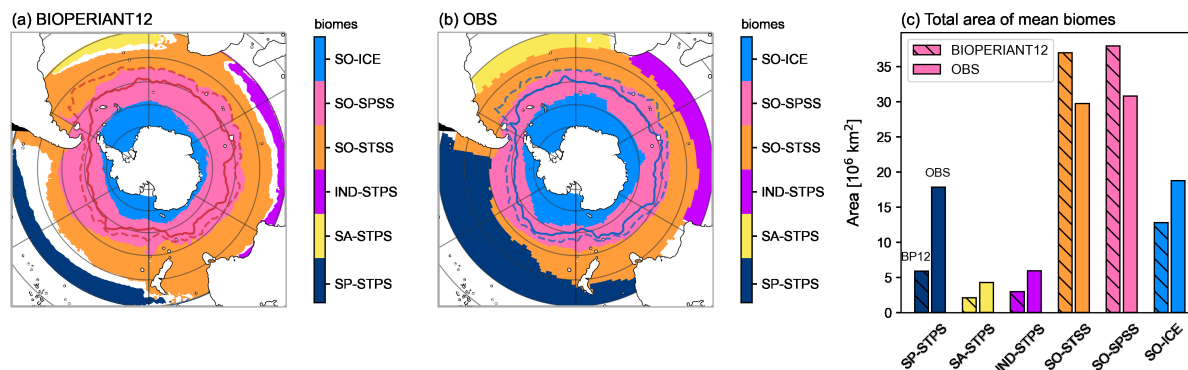


Figure 6. SO mean biome boundaries for (a) BIOPERIANT12 using the biome criteria definitions from Fay and McKinley (2014), (b) the observation-based mean biome dataset of Fay and McKinley (2014) south of 30° S (see Supplementary). (c) Total area per biome for BIOPERIANT12 (hatched bars, titled BP12) and for the dataset (plain bars, titled OBS). In the SO (below 30° S), six biomes are identified: the ice biome (SO-ICE), the subpolar seasonally stratified biome (SO-SPSS), the subtropical seasonally stratified biome (SO-STSS) and the Indian, South Atlantic, and South Pacific subtropical permanently stratified biome (IND-STPS, SA-STPS and SP-STPS respectively).

could be associated with the high mesoscale spatial and temporal variability (low seasonality of 0.12) in the model compared with data. While in the SO-ICE biome, high variability in salinity (RSD=1.55), MLD (RSD =1.56) as well as dissolved O_2 (RSD=1.66), point at the influential role of sea ice and freshwater dynamics in the model region and suggest improvement or further investigation. For the BGC, poor model reliability for carbon, silicate, and chlorophyll as well as deviations in nutrients will be addressed in the proceeding sections.



Table 3. Seasonal cycle surface climatology per biome: BIOPERIANT12 (BP12) vs observations (OBS): area-weighted Mean and Amplitude (difference between maximum and minimum) for the respective data sources; SCR seasonal cycle reproducibility (the correlation of the interannual varying timeseries against its climatological seasonal cycle) where temporal resolution allows; and for comparison Correlation (correlation coefficient), RSD (ratio of BP12:OBS standard deviation), Model Reliability Index (log-transform error).

		Variable								Variable					
		SO-ICE		SO-SPSS		SO-STSS				SO-ICE		SO-SPSS		SO-STSS	
	Biome	BP12	OBS	BP12	OBS	BP12	OBS		Biome	BP12	OBS	BP12	OBS	BP12	OBS
Temperature [°C]	Mean	-1.49	-1.00	3.03	3.76	13.45	12.75	Salinity	Mean	34.03	33.96	34.01	33.93	34.83	34.71
	Amplitude	1.16	1.82	2.36	2.74	3.90	4.25		Amplitude	0.70	0.43	0.08	0.08	0.01	0.06
	SCR	0.63		0.71		0.54			SCR	0.35		0.20		0.12	
	Correlation		0.94		0.98		0.99		Correlation		0.99		0.84		0.62
	RSD	0.66		0.90		0.93			RSD	1.55		1.07		0.14	
	Model RI	2.32		1.26		1.06			Model RI	1.00		1.00		1.00	
MLD [m]	Mean	66.72	57.02	109.79	109.08	86.20	100.53	Tot. chl-a [mgm ⁻³]	Mean	0.58	0.28	0.51	0.24	0.61	0.35
	Amplitude	86.87	54.57	143.26	118.04	153.40	158.03		Amplitude	1.69	0.70	0.88	0.23	0.75	0.21
	SCR	0.76		0.74		0.75			SCR	0.88	0.36	0.85	0.36	0.68	0.21
	Correlation		0.86		1.00		1.00		Correlation		0.93		0.86		0.91
	RSD	1.56		1.19		0.95			RSD	2.37		4.22		3.64	
	Model RI	1.41		1.11		1.31			Model RI	1.86		2.10		1.69	
pCO ₂ [µatm]	Mean	345.25	367.37	363.98	365.15	362.96	345.27	FCO ₂ [molm ⁻² yr ⁻¹]	Mean	-0.82	0.15	-1.12	-0.07	-0.77	-1.81
	Amplitude	49.30	47.90	10.22	17.10	13.08	11.85		Amplitude	2.17	1.80	1.17	1.48	1.54	0.45
	SCR	0.79	0.79	0.59	0.80	0.51	0.83		SCR	0.39	0.77	0.31	0.80	0.28	0.76
	Correlation		0.89		-0.45		-0.59		Correlation		0.89		-0.78		-0.23
	RSD	0.91		0.65		1.06			RSD	1.30		0.80		3.53	
	Model RI	1.07		1.02		1.06			Model RI	3.87		2.59		6.37	
DIC [µmolkg ⁻¹]	Mean	2181.93	2148.95	2151.61	2123.52	2087.99	2056.03	Tot. Alkalinity [µmolkg ⁻¹]	Mean	2303.80	2295.51	2295.77	2281.70	2317.60	2300.31
	Amplitude	62.96	0.00	15.50	0.00	23.00	0.00		Amplitude	43.62	0.00	3.67	0.00	4.02	0.00
	SCR	0.53		0.44		0.47			SCR	0.50		0.29		0.21	
	Correlation				0.00		0.00		Correlation		-0.00				
	RSD								RSD						
	Model RI	1.02		1.01		1.02			Model RI	1.01		1.01		1.01	
Nitrate [mmol ⁻¹]	Mean	26.02	25.73	23.04	21.75	10.52	6.83	Phosphate [mmol ⁻¹]	Mean	1.85	1.81	1.63	1.56	0.80	0.68
	Amplitude	3.92	3.69	1.91	2.73	3.77	3.52		Amplitude	0.22	0.26	0.10	0.32	0.21	0.33
	SCR	0.58		0.46		0.61			SCR	0.56		0.42		0.55	
	Correlation		0.95		0.95		0.97		Correlation		0.99		0.90		0.92
	RSD	1.28		0.73		1.24			RSD	0.86		0.36		0.67	
	Model RI	1.02		1.06		1.55			Model RI	1.03		1.07		1.22	
Silicate [mmol ⁻¹]	Mean	48.47	53.42	26.46	15.85	5.81	3.37	Diss. O ₂ [µmol ⁻¹]	Mean	357.13	347.78	332.14	326.98	264.86	274.04
	Amplitude	13.96	12.44	5.47	11.30	2.70	2.70		Amplitude	29.65	21.34	13.77	14.52	17.08	16.90
	SCR	0.64		0.49		0.62			SCR	0.53		0.45		0.47	
	Correlation		0.85		0.96		0.95		Correlation		0.86		0.94		0.99
	RSD	1.18		0.49		1.05			RSD	1.66		0.91		0.95	
	Model RI	1.12		1.79		1.79			Model RI	1.03		1.02		1.03	

^a GLODAPv2 observations are an annual mean product.

RSD:SD of BP12 greater (less) than that of OBS by factor 1.5 (0.5). **Correlation:** BP12-OBS correlation coefficient less than 0.5.

SCR: BP12 greater than 0.65 (medium to high). **Model RI:** greater 1.5 (medium to high).

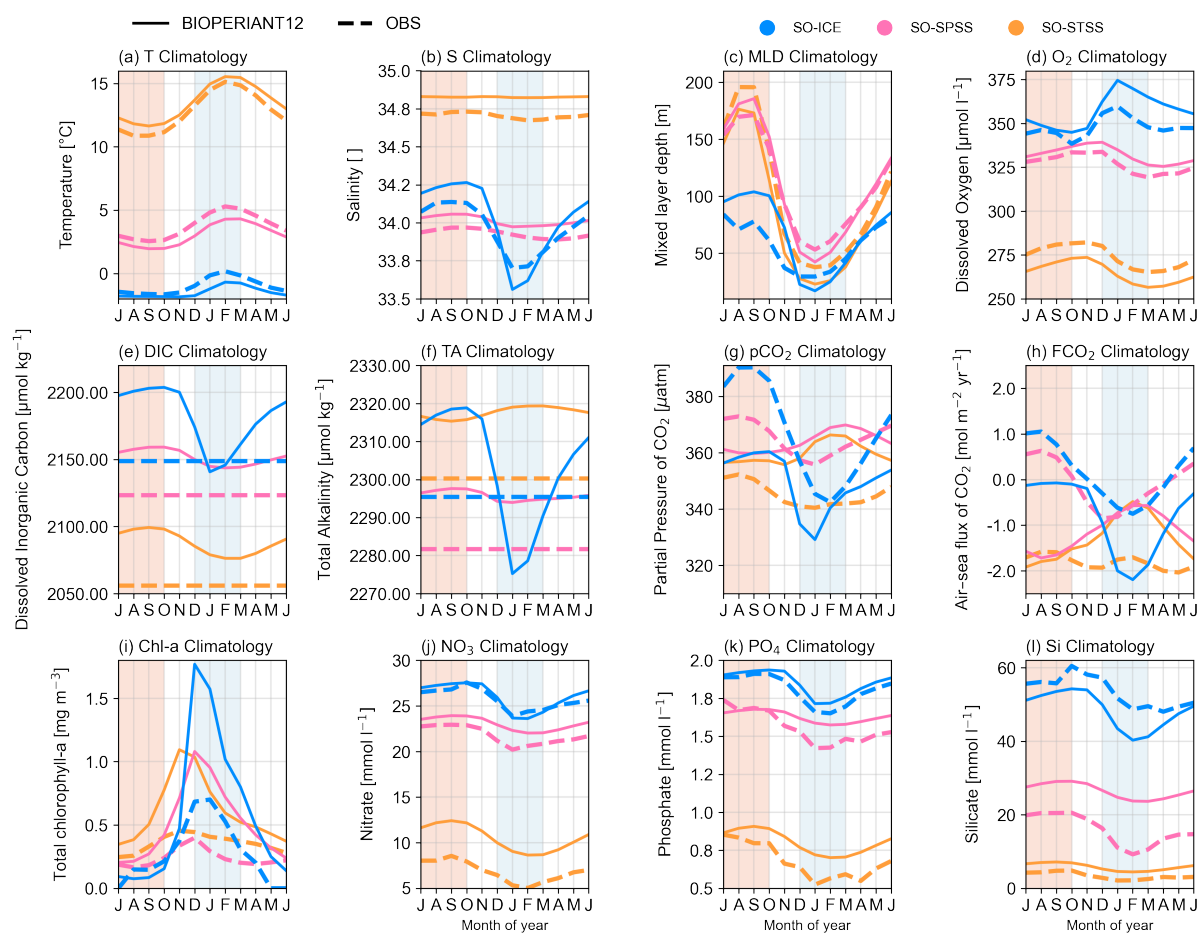


Figure 7. BIOPERIANT12 model (solid line) versus Observations (dashed line) surface seasonal cycle (2000–2009 climatology) spatially averaged per biome for selected variables. Biomes include SO-ICE (blue), SO-SPSS (pink) and SO-STSS (orange) corresponding to map in Fig. 6.



3.3 Carbon

Recent studies have highlighted the importance of resolving intra-seasonal to seasonal modes of variability for both anthropogenic and natural carbon fluxes in order to reduce the uncertainties of the mean annual fluxes and strengthen model projections (DeVries et al., 2023; Rustogi et al., 2023). Using SCR, as a metric of variability, a comparison of the SCR of pCO₂ in BIOPERIANT12 against the monthly, data product CSIR-ML6 (Fig. 8) shows that model pCO₂ for the SO-STSS and SO-SPSS biomes are dominated by large regions of interannual variability (SCR=0.59, 0.51, respectively) aligned with regions of high EKE (Fig. 2) which are not captured by the monthly CSIR-ML6 product (Fig. 8c). CSIR-ML6, instead, displays high seasonality in all three SO biomes with SCR 0.80, 0.80, 0.79 in the SO-STSS, SO-SPSS, SO-ICE biomes, respectively (Table 3), i.e. driven by seasonal surface fluxes and ice (although the monthly temporal resolution may contribute to this).

This results in dissimilar pCO₂ seasonal cycles (Fig. 7g) highlighted by weak correlations in the SO-STSS and SO-SPSS biomes (R=-0.59, -0.45, respectively) whilst showing good model–data agreement in the SO-ICE biome; a region that is also strongly seasonally driven in the model (SCR=0.79, for both model and data) and with coherent model–data phasing (R=0.89), although minima are one month out of phase. Despite biome mean differences in the model climatology, we calculate a small model–data bias of pCO₂ for all 3 biomes indicated by model RI between 1.02 to 1.07, which suggests that BIOPERIANT12 is in agreement with the data product CSIR-ML6; also shown in the Probability Density Functions (PDFs) for pCO₂ for the SO domain mean (Fig. S13a). This emphasises the importance of mesoscale-resolving model resolution in the SO, in capturing the variability of CO₂.

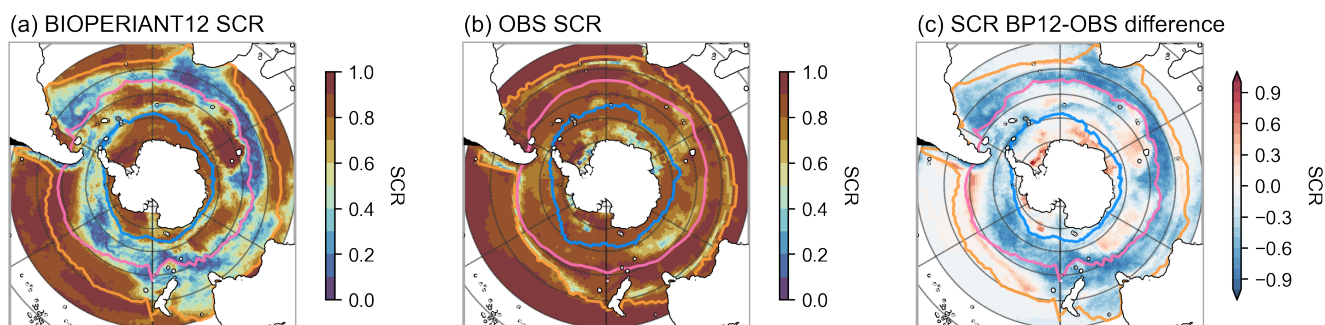


Figure 8. Seasonal cycle reproducibility of pCO₂ for (a) BIOPERIANT12, (b) CSIR-ML6 observation based reconstruction, and (c) model–data difference. Maps are overlaid with the northern climatological biome borders corresponding to model/data SO biomes.

The spatial distribution of pCO₂ shown in Fig. 9 (a–f) reflects the seasonality differences between model and data, showing the overestimation of model versus data pCO₂ in the SO-STSS and underestimation in the SO-ICE biomes. Differences in seasonal cycle phasing in the SO-SPSS and SO-STSS biomes are clearly seen in the interannual time series (Fig. 9i, k) with model peaks in summer compared to winter peaks in the data. The PDFs for pCO₂ (Fig. 9h, j, l) show a general wider distribution (higher standard deviation) in the model biomes and not the distinct inter-biome differences shown in the data, such as the narrow pCO₂ distribution in the SO-SPSS (Fig. 9j).



The seasonal cycle differences of $p\text{CO}_2$ (and FCO_2) in the model SO-SPSS and SO-STSS biomes relative to these observations may be representative of different mechanisms. The $p\text{CO}_2$ seasonal maximum in summer (JFM) is in phase with temperature maximum (Fig. 7a) but out of phase with the chlorophyll peak 2 months earlier (OND) (Fig. 7i, 13) and associated nutrient decrease (NO_3 and Si, Fig. 7j, l). This is consistent with the model's $p\text{CO}_2$ seasonal cycle in the SO-SPSS and SO-STSS biomes being primarily regulated by the thermal component of $p\text{CO}_2$ (Mongwe et al., 2016). On the other hand, there is better model–data phasing of the seasonal cycles of $p\text{CO}_2$ and FCO_2 in the SO-ICE biome (Fig. 7g, h). Additionally, temperature, chlorophyll, and nutrient model-data seasonal cycles are comparable in phase (Fig. 7i–l). However, the amplitude of the BIOPERIANT12 seasonal chlorophyll maximum is double that of the observed estimate (due to regions of high chlorophyll, Fig. 11) which may result in a larger contribution of the biological components driving $p\text{CO}_2$ as compared to the thermally driven ice free regions.

It is noted that observational products, particularly underway $p\text{CO}_2$ observations used in reconstructions, have significant seasonal biases themselves, as they are based on limited observations during winter. Thus, the magnitude and direction of the observed seasonal cycle of $p\text{CO}_2$ and FCO_2 in the SO is still under investigation (Gray et al., 2018; Landschützer et al., 2018; Gregor et al., 2019; Gruber et al., 2019; Bushinsky et al., 2019; Mackay and Watson, 2021). The seasonal biases in these products may also manifest as artificial variability on longer time scales (Hauck et al., 2023). The poor representation of biological processes of the SO-SPSS and SO-STSS in the model contributing to differences in the $p\text{CO}_2$ (and FCO_2) seasonal cycles is discussed in the Supplementary. We propose that a weaker seasonal vertical flux in DIC as shown by the smooth upper ocean DIC gradient compared to the dataset (Fig. S11) leads to a weaker DIC entrainment potential during the seasons of enhanced vertical mixing, and hence a diminished seasonal DIC variability (Mongwe et al., 2016).

3.4 Biogeochemistry

3.4.1 Dissolved Iron

Dissolved iron (dFe) limits phytoplankton growth across the surface of the SO, impacting the functioning of marine ecosystems and thus the carbon cycle. It is thus imperative that models adequately represent the spatial and seasonal distribution of dFe. In the SO, dFe is notoriously undersampled, it occurs at small (nanomolar, n M) concentrations and its complex chemistry makes it difficult to observe. Here, we compare BIOPERIANT12 with a compilation of dFe observations collated by Tagliabue et al. (2012) over 2000–2009 (Fig. 10). BIOPERIANT12 simulates the observed spatial distribution of upper ocean dFe concentrations, with higher concentrations > 0.4 n M close to coastal boundaries, downstream and around subAntarctic islands (particularly evident for Kerguelen), and in the vicinity of the Agulhas Retroflexion (Fig. 10a, c). Far from the influence of land masses, the simulated dFe concentrations are lower < 0.3 n M, as similarly seen in the observations (Fig. 10b). In general, the simulated range of upper dFe is on the lower end of the range of the observations; it has been noted that PISCES tends to exaggerate the low dFe concentrations in the open ocean of the SO (Aumont et al., 2015).

The shape of the vertical profile of dFe is important as it plays a fundamental role in how much dFe is available to be supplied to the surface i.e. via deep winter convective mixing and by mesoscale eddies (Tagliabue et al., 2014; Nicholson

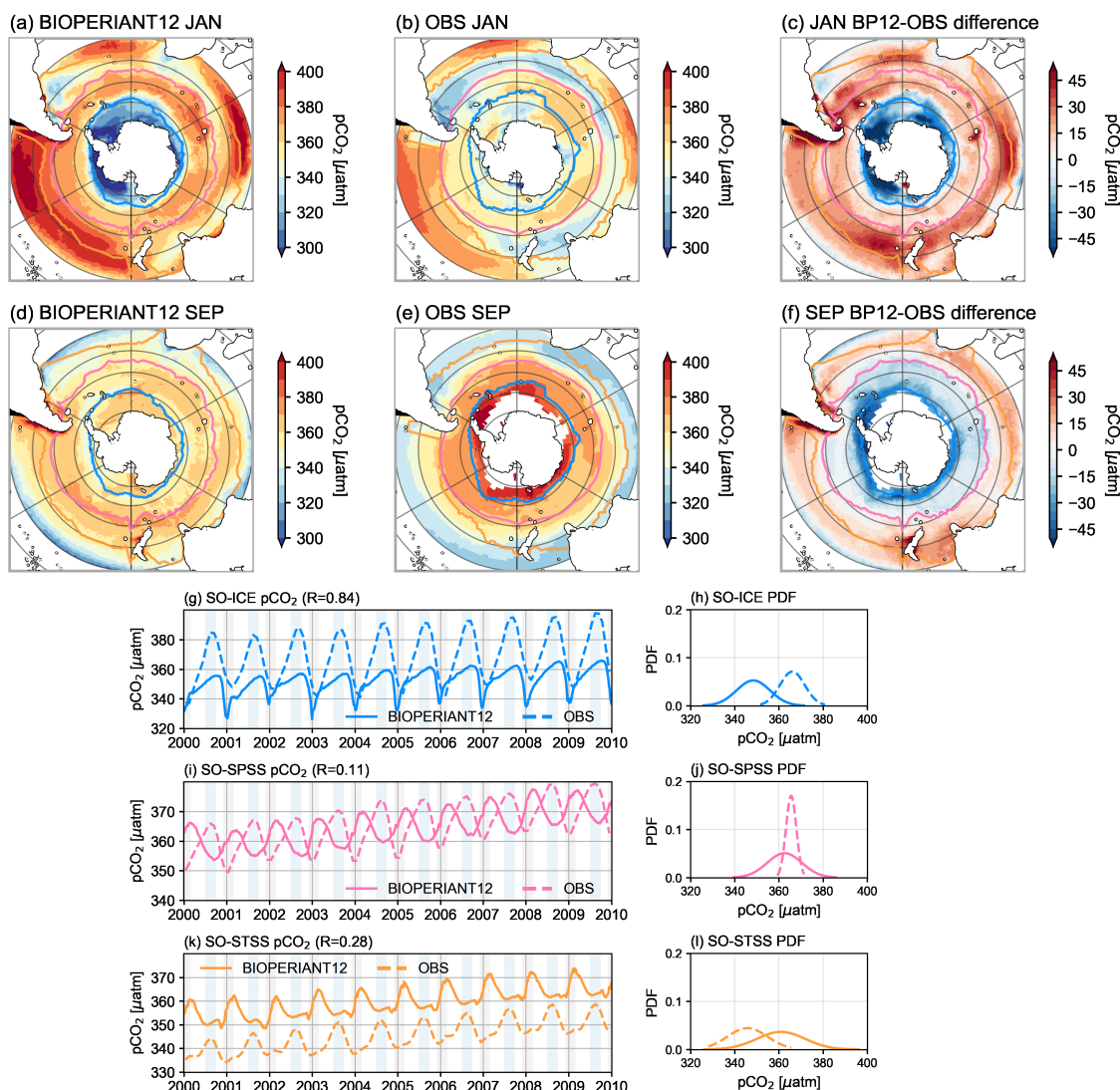


Figure 9. Seasonal comparison of pCO₂ for (a, d) BIOPERIANT12, and (b, e) CSIR-ML6 observation based dataset, and (c, f) model–data difference, for January and September monthly climatology, respectively. Maps are overlaid with the northern climatological biome borders corresponding to model/data SO biomes. Evolution of area-weighted pCO₂ for model versus data and corresponding PDF for (g, h) SO-ICE, (h, i) SO-SPSS, and (k, l) SO-STSS biomes.

et al., 2019). BIOPERIANT12 is able to simulate the mean observed characteristics of a general dFe profile (Fig. 10e) with low concentrations between 0-100 m due to biological consumption and increasing DFe concentrations with depth due to remineralization of sinking organic material. The simulated mean range dFe compares relatively well with mean observations over the upper 500 m. Below this, the simulated mean range is lower. The lack of measurements during key seasonal transitions



particularly over winter (Fig. 10f) make comparisons of the simulated seasonal distribution of surface dFe difficult. However, during austral summer (DJF), dFe is expected to be low due to biological consumption from spring to summer and during winter (JJA), dFe is expected to be higher due to deep convective mixing entraining subsurface dFe to the surface (Tagliabue et al., 2012) These seasonal differences are simulated by BIOPERIANT12 (Fig. 10f) and are particularly evidenced by the summer and winter snapshots in Fig. 10c and d, respectively.

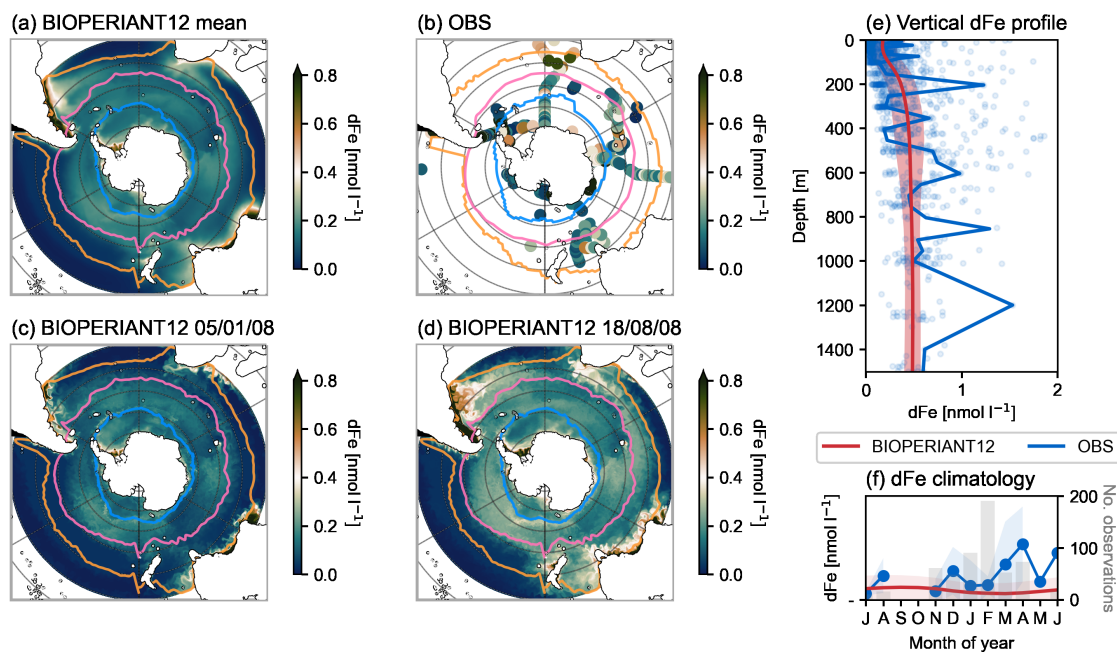


Figure 10. Surface (0-50 m) dissolved iron (dFe) concentration for (a) BIOPERIANT12 climatological annual mean (b) observations obtained during years 2000-2009 (Tagliabue et al., 2012). Seasonal snapshots of BIOPERIANT12 dFe for (c) summer (5 January 2008) and (d) winter (18 August 2008). (e) Annual mean vertical distribution of dFe for BIOPERIANT12 without area-weighting (red line = mean, red shading = spatial standard deviation) and observations (blue). (f) Model versus observation monthly mean climatology (line) and standard deviation (shading). The number of observations in each month is shown by grey bars.

3.4.2 Nutrients

Model RI values in Table 3 show that the model is able to reasonably reproduce the seasonal climatology of NO_3 and PO_4 with relatively comparable seasonal cycles (Fig. 7), particularly for the more southern biomes (e.g. RI values between 1.02 and 1.07 for both NO_3 and PO_4 in the SO-ICE and SO-SPSS biomes). However, simulated surface silicate is less well represented by the model (SO-SPSS and SO-STSS both $\text{RI}=1.79$): in the SO-SPSS, model silicate means differ compared to data (26.46 vs. 15.85 mmol l^{-1}), considering their amplitudes (5.47 vs. 11.3 mmol l^{-1}) and variability that is half that of the data (model $\text{RSD}=0.49$). These differences may result from the representation of simulated silicate due to uncertainty in laboratory experiments as noted



in Aumont et al. (2015). This may affect the concentration of diatoms in the model. PO_4 variability in the model is also low, 0.36 times that expected of data however, with comparable means. It is important to note that much of the observational data is
385 collected during the productive season (austral summer) in the SO, and thus surface values observed may be biased towards
lower values (Fig. 7, S16). However, deeper in the water column at 200 m (Table S1, Fig. S17), RIs for the 3 aforementioned
nutrients reflect a good agreement between the model and observations at this level (between 1.00 and 1.30). Model nutrients
at this depth are stable, standard deviations smaller than from the data climatology as in the vertical profiles (Fig. S11). Over
the evolution of the model (Fig. S16 and S17), there is a slight decreasing trend in nutrients, particularly noticeable in the
390 SO-SPSS at the surface and 200 m and should be taken into account in process studies.

3.4.3 Surface chlorophyll

BIOPERIANT12 represents the main spatial surface patterns of regions of higher and lower surface chlorophyll as compared to
OC-CCIv6 satellite-derived chlorophyll concentrations (Fig. 11). For example, it simulates the higher surface chlorophyll close
to continental margins and in the region of ocean fronts such as in the SAZ (not shown), while low chlorophyll is simulated
395 in more oligotrophic regions such as the SO Pacific. However, the spatial extent of enhanced chlorophyll regions associated
with shallow topography are larger in the model. The incorporation of these regions within the biome definitions contribute to
the magnitude of the surface chlorophyll which is overestimated in BIOPERIANT12, with variability over double that of the
observations in all biomes (RSD greater than 2 in Table 3).

SCR (Fig. 12) suggests that the drivers of the differences are from dynamics as model chlorophyll is seasonally driven
400 while the data product suggests that drivers are on the intraseasonal time-scale. Despite this, the seasonal cycle for the SO
biomes correlates well with data. A comparison of the simulated biome-mean seasonal cycle against observations of OC-
CCIv6 chlorophyll for each biome (Fig. 13a–c, S18) shows good agreement of the timing of the bloom maximum in December
(date difference within 14 days). However, the general characteristics, such as initiation and termination date defined using
the biomass threshold method of 5 % (Ryan-Keogh et al., 2023) only compare well for the SO-STSS region, both initiating
405 in August and terminating in May. For the SO-SPSS biome, both the model and observation blooms start in September and
while OC-CCIv6 blooms terminate in March, the model sustains the bloom a further 93 days into June. In contrast, the SO-ICE
biome bloom for both sources terminate in May, while the simulated bloom starts 3 months after observations (October vs.
August).

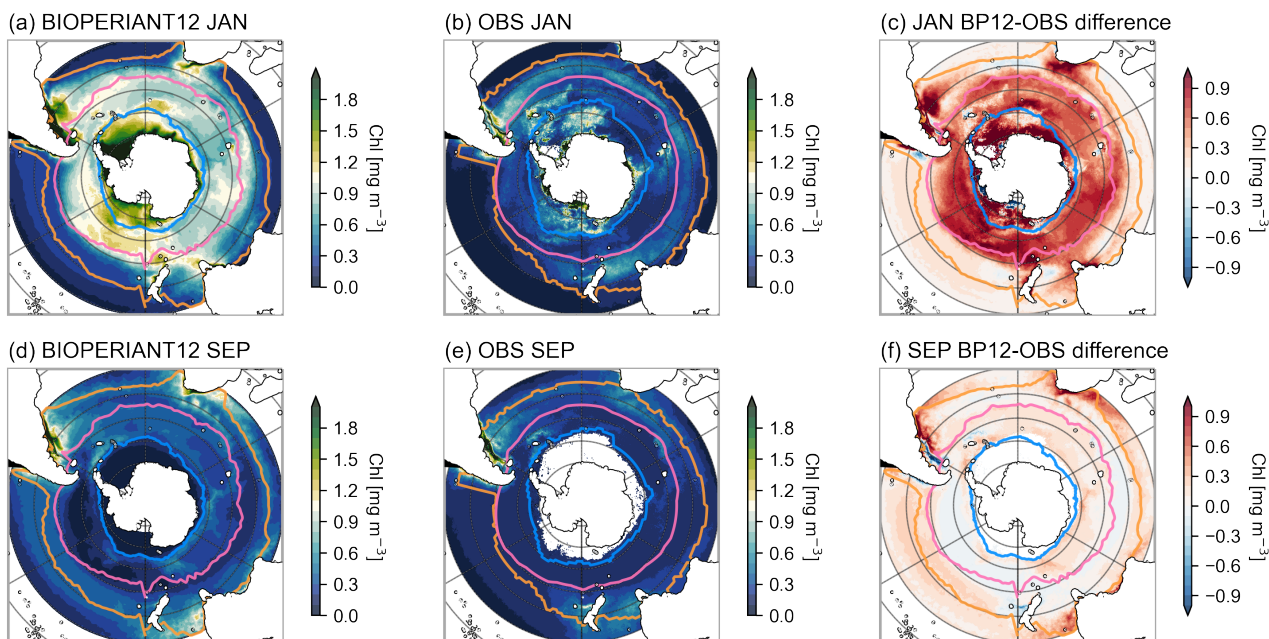


Figure 11. Climatological mean total chlorophyll concentrations for (a, b) BIOPERIANT12 vs (d, e) OC-CCI observation-based product for January and September. SCR of surface chlorophyll for (c)BIOPERIANT12 and (f) observations. Model versus observation seasonal cycle of surface chlorophyll for (g) SO-ICE, (h) SO-SPSS, and (i) SO-STSS biomes.

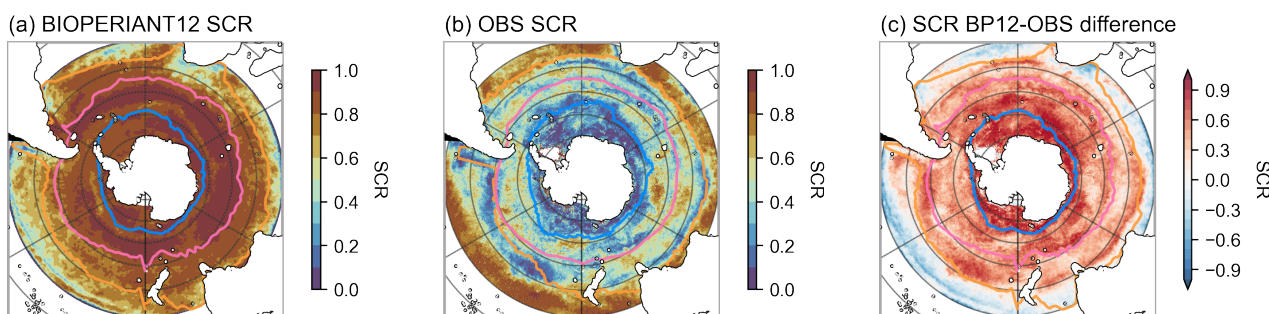


Figure 12. Seasonal cycle reproducibility (SCR) of surface chlorophyll concentration for (a) BIOPERIANT12, (b) OC-CCIv6 observation-based product, and (c) model-observation SCR bias.

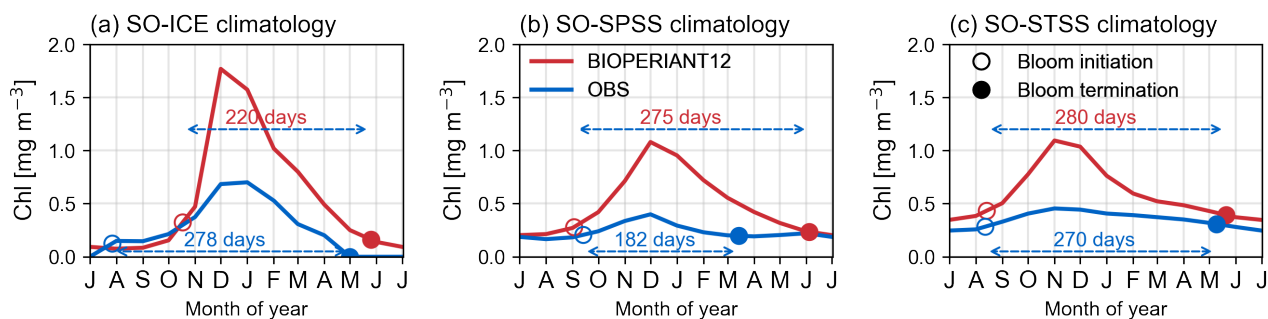


Figure 13. BIOPERIANT12 model versus OC-CCI observation climatological bloom characteristics overlaid on the seasonal cycle of surface chlorophyll for (a) SO-ICE, (b) SO-SPSS, and (c) SO-STSS biomes.



4 Conclusions

410 The complex dynamics of the SO has been scrutinised in many papers, particularly with its role in the climate system and influence on carbon projections by ESMs. While inter-model comparisons may show the weaknesses and strengths, the models themselves are also complex systems defined by multiple interacting parts defined by many assumptions, making isolating biases challenging. BIOPERIANT12, on the other hand, while composed of the major components of ocean, ice and biogeochemistry, provides a simpler, stable reference model with a reasonable mean state with which we can address process
415 questions, diagnose model biases, and build future model experiments. Despite the eddy resolution, the simulated SO seasonal cycle still needs improvement. Model-observation differences, not addressed in this evaluation paper, can lead to further paths of enquiry.

The importance of the mesoscale on biology in the SO requires particular attention with the local environment of the phytoplankton modified through both biological and physical mechanisms, for example by altering gradients and adjusting access
420 to light and nutrients which affect growth and hence the biological carbon pump. Large biomass anomalies in both spatial and seasonally variability are reported in Rohr et al. (2020). In BIOPERIANT12, chlorophyll variability from two phytoplankton classes (nanophytoplankton and diatoms), averaged over biomes, exceeded observational values by more than double. In the SO, where biological processes play an important role in carbon exchange, the simulated processes which give rise to these high values need to be explored. Despite the magnitude differences, the temporal variability should also be addressed, the
425 SCR shows that the simulated chlorophyll response is driven by strong seasonal factors, when a higher-temporal response is expected as displayed by the OC-CCIV6 data.

BIOPERIANT12 provides a stable, coherent 3-dimensional evolving dataset at relatively high resolution to test sampling strategies and biases, such as investigating the uncertainties in the $p\text{CO}_2$ in the SO (Djeutchouang et al., 2022) or examining the relationship between cyclonic and anticyclonic eddies in the South Atlantic-SO on heat and carbon (Smith et al., 2023).

430 Unfortunately, the computational requirements of this configuration with coupled physics-ice-BGC make sensitivity studies of long duration unrealistic. However, model-observation disagreements provided by BIOPERIANT12 suggest regions where the model configuration was poorly designed or missing processes that warrant further investigation. These will be explored with higher resolution, more appropriate datasets. Some may be addressed with newer versions of the model.

Code and data availability. The model configuration is available at <https://doi.org/10.5281/zenodo.13910093>. Code and data used for visu-
435 alisations in this manuscript are available on

Author contributions. Model configuration, production: NC, TCM. Analysis, visualisation, software: NC, SN, MdP, AL, TM. Writing - original draft: NC. Writing, reviewing, editing: all authors.



Competing interests. There are no competing interests to declare.

Acknowledgements. The authors acknowledge their institutional support from the CSIR Parliamentary Grant (0000005278) and the Department of Science and Innovation. SN, NC acknowledges the National Research Foundation South African National Antarctic Programme (SANAP200324510487, SANAP230503101416). PM was also funded by the European Union's Horizon 2020 research 535 and innovation programme under grant agreement No. 820989 (COMFORT). We gratefully acknowledge the Centre for High-Performance Computing (NICIS-CHPC) for providing the computational resources for the development, production, and analysis of BIOPERIANT12. NC extends appreciation to their dedicated team for their invaluable support throughout this challenging process. Additionally, NC has benefited from the expertise and support of A. Albert, J.-M. Molines, and J. Le Sommer at Laboratoire de Glaciologie et Gèophysique de l'Environnement (LGGE), Grenoble through the Marie-Curie International Research Staff Exchange Scheme, SOCCLi (The role of the Southern Ocean Carbon cycle under CLimate change, FP7-PEOPLE-2012-IRSES, 2012-2016).



References

- Abernathy, R. P., Cerovecki, I., Holland, P. R., Newsom, E., Mazloff, M., and Talley, L. D.: Water-Mass Transformation by Sea Ice in the
450 Upper Branch of the Southern Ocean Overturning, *Nature Geoscience*, 9, 596–601, <https://doi.org/10.1038/ngeo2749>, 2016.
- Anav, A., Friedlingstein, P., Kidston, M., Bopp, L., Ciais, P., Cox, P., Jones, C., Jung, M., Myneni, R., and Zhu, Z.: Evaluating the
Land and Ocean Components of the Global Carbon Cycle in the CMIP5 Earth System Models, *Journal of Climate*, 26, 6801–6843,
<https://doi.org/10.1175/JCLI-D-12-00417.1>, 2013.
- Aumont, O. and Bopp, L.: Globalizing Results from Ocean in Situ Iron Fertilization Studies, *Global Biogeochemical Cycles*, 20,
455 <https://doi.org/10.1029/2005GB002591>, 2006.
- Aumont, O., Ethé, C., Tagliabue, A., Bopp, L., and Gehlen, M.: PISCES-v2: An Ocean Biogeochemical Model for Carbon and Ecosystem
Studies, *Geoscientific Model Development*, 8, 2465–2513, <https://doi.org/10.5194/gmd-8-2465-2015>, 2015.
- Barnier, B., Blaker, A., Biatosch, A., Boening, C., Coward, A., Deshayes, J., Hirshi, J., Sommer, J., Madec, G., Maze, G., Molines, J.,
New, A. L., Penduff, T., Scheinert, M., Talandier, C., and Treguier, A.: DRAKKAR: Developing High Resolution Ocean Components for
460 European Earth System Models, CLIVAR Exchanges, 2014.
- Beadling, R. L., Russell, J. L., Stouffer, R. J., Mazloff, M., Talley, L. D., Goodman, P. J., Sallée, J. B., Hewitt, H. T., Hyder, P., and Pandde,
A.: Representation of Southern Ocean Properties across Coupled Model Intercomparison Project Generations: CMIP3 to CMIP6, *Journal
of Climate*, 33, 6555–6581, <https://doi.org/10.1175/JCLI-D-19-0970.1>, 2020.
- Bushinsky, S. M., Landschützer, P., Rödenbeck, C., Gray, A. R., Baker, D., Mazloff, M. R., Resplandy, L., Johnson, K. S., and Sarmiento,
465 J. L.: Reassessing Southern Ocean Air–Sea CO₂ Flux Estimates With the Addition of Biogeochemical Float Observations, *Global Bio-
geochemical Cycles*, 33, 1370–1388, <https://doi.org/10.1029/2019GB006176>, 2019.
- Chapman, C. C.: New Perspectives on Frontal Variability in the Southern Ocean, *Journal of Physical Oceanography*, 47, 1151–1168,
<https://doi.org/10.1175/JPO-D-16-0222.1>, 2017.
- Chassignet, E. P., Yeager, S. G., Fox-Kemper, B., Bozec, A., Castruccio, F., Danabasoglu, G., Horvat, C., Kim, W. M., Koldunov, N., Li,
470 Y., Lin, P., Liu, H., Sein, D. V., Sidorenko, D., Wang, Q., and Xu, X.: Impact of Horizontal Resolution on Global Ocean–Sea Ice Model
Simulations Based on the Experimental Protocols of the Ocean Model Intercomparison Project Phase 2 (OMIP-2), *Geoscientific Model
Development*, 13, 4595–4637, <https://doi.org/10.5194/gmd-13-4595-2020>, 2020.
- Daniault, N. and Ménard, Y.: Eddy Kinetic Energy Distribution in the Southern Ocean from Altimetry and FGGE Drifting Buoys, *Journal of
Geophysical Research: Oceans*, 90, 11 877–11 889, <https://doi.org/10.1029/JC090iC06p11877>, 1985.
- 475 de Boyer Montégut, C., Madec, G., Fischer, A., Lazar, A., and Iudicone, D.: Mixed layer depth over the global ocean: An examination of
profile data and a profile-based climatology, *Journal of Geophysical Research*, 109, 2004.
- Dee, D. P., Uppala, S. M., Simmons, A. J., Berrisford, P., Poli, P., Kobayashi, S., Andrae, U., Balmaseda, M. A., Balsamo, G., Bauer,
P., Bechtold, P., Beljaars, A. C. M., van de Berg, L., Bidlot, J., Bormann, N., Delsol, C., Dragani, R., Fuentes, M., Geer, A. J., Haim-
berger, L., Healy, S. B., Hersbach, H., Hólm, E. V., Isaksen, L., Kållberg, P., Köhler, M., Matricardi, M., McNally, A. P., Monge-Sanz,
480 B. M., Morcrette, J.-J., Park, B.-K., Peubey, C., de Rosnay, P., Tavolato, C., Thépaut, J.-N., and Vitart, F.: The ERA-Interim Reanalysis:
Configuration and Performance of the Data Assimilation System, *Quarterly Journal of the Royal Meteorological Society*, 137, 553–597,
<https://doi.org/10.1002/qj.828>, 2011.



- DeVries, T., Yamamoto, K., Wanninkhof, R., Gruber, N., Hauck, J., Müller, J. D., Bopp, L., Carroll, D., Carter, B., Chau, T.-T.-T., et al.: Magnitude, trends, and variability of the global ocean carbon sink from 1985 to 2018, *Global Biogeochemical Cycles*, 37, e2023GB007780, 485 2023.
- Dietze, H., Löptien, U., and Getzlaff, J.: MOMSO 1.0 – an Eddyding Southern Ocean Model Configuration with Fairly Equilibrated Natural Carbon, *Geoscientific Model Development*, 13, 71–97, <https://doi.org/10.5194/gmd-13-71-2020>, 2020.
- Djeutchouang, L. M., Chang, N., Gregor, L., Vichi, M., and Monteiro, P. M. S.: The Sensitivity of $p\text{CO}_2$ Reconstructions to Sampling Scales across a Southern Ocean Sub-Domain: A Semi-Idealized Ocean Sampling Simulation Approach, *Biogeosciences*, 19, 4171–4195, 490 <https://doi.org/10.5194/bg-19-4171-2022>, 2022.
- Doney, S. C., Lima, I., Moore, J. K., Lindsay, K., Behrenfeld, M. J., Westberry, T. K., Mahowald, N., Glover, D. M., and Takahashi, T.: Skill Metrics for Confronting Global Upper Ocean Ecosystem-Biogeochemistry Models against Field and Remote Sensing Data, *Journal of Marine Systems*, 76, 95–112, <https://doi.org/10.1016/j.jmarsys.2008.05.015>, 2009.
- Dong, S., Sprintall, J., and Gille, S. T.: Location of the Antarctic Polar Front from AMSR-E Satellite Sea Surface Temperature Measurements, 495 *Journal of Physical Oceanography*, 36, 2075–2089, <https://doi.org/10.1175/JPO2973.1>, 2006.
- Dong, S., Sprintall, J., Gille, S. T., and Talley, L.: Southern Ocean mixed-layer depth from Argo float profiles, *Journal of Geophysical Research: Oceans*, 113, <https://doi.org/10.1029/2006JC004051>, _eprint: <https://onlinelibrary.wiley.com/doi/pdf/10.1029/2006JC004051>, 2008.
- Donohue, K. A., Kennelly, M. A., and Cutting, A.: Sea Surface Height Variability in Drake Passage, *Journal of Atmospheric and Oceanic* 500 *Technology*, 33, 669–683, <https://doi.org/10.1175/JTECH-D-15-0249.1>, 2016.
- Downes, S. M., Farneti, R., Uotila, P., Griffies, S. M., Marsland, S. J., Bailey, D., Behrens, E., Bentsen, M., Bi, D., Biastoch, A., Böning, C., Bozec, A., Canuto, V. M., Chassignet, E., Danabasoglu, G., Danilov, S., Diansky, N., Drange, H., Fogli, P. G., Gusev, A., Howard, A., Ilicak, M., Jung, T., Kelley, M., Large, W. G., Leboissetier, A., Long, M., Lu, J., Masina, S., Mishra, A., Navarra, A., George Nurser, A., Patara, L., Samuels, B. L., Sidorenko, D., Spence, P., Tsujino, H., Wang, Q., and Yeager, S. G.: An assessment of 505 Southern Ocean water masses and sea ice during 1988–2007 in a suite of interannual CORE-II simulations, *Ocean Modelling*, 94, 67–94, <https://doi.org/10.1016/j.ocemod.2015.07.022>, 2015.
- du Plessis, M. D., Swart, S., Biddle, L. C., Giddy, I. S., Monteiro, P. M. S., Reason, C. J. C., Thompson, A. F., and Nicholson, S.-A.: The Daily-Resolved Southern Ocean Mixed Layer: Regional Contrasts Assessed Using Glider Observations, *Journal of Geophysical Research: Oceans*, 127, e2021JC017760, <https://doi.org/10.1029/2021JC017760>, 2022.
- 510 Dufour, C. O., Le Sommer, J., Zika, J. D., Gehlen, M., Orr, J. C., Mathiot, P., and Barnier, B.: Standing and Transient Eddies in the Response of the Southern Ocean Meridional Overturning to the Southern Annular Mode, *Journal of Climate*, 25, 6958–6974, <https://doi.org/10.1175/JCLI-D-11-00309.1>, 2012.
- Dufour, C. O., Sommer, J. L., Gehlen, M., Orr, J. C., Molines, J.-M., Simeon, J., and Barnier, B.: Eddy Compensation and Controls of the Enhanced Sea-to-Air CO_2 Flux during Positive Phases of the Southern Annular Mode: CO_2 FLUX RESPONSE TO SAM, *Global* 515 *Biogeochemical Cycles*, 27, 950–961, <https://doi.org/10.1002/gbc.20090>, 2013.
- Fay, A. R. and McKinley, G. A.: Global Open-Ocean Biomes: Mean and Temporal Variability, *Earth System Science Data*, 6, 273–284, <https://doi.org/10.5194/essd-6-273-2014>, 2014.
- Freeman, N. M. and Lovenduski, N. S.: Mapping the Antarctic Polar Front: weekly realizations from 2002 to 2014, *Earth System Science Data*, 8, 191–198, <https://doi.org/10.5194/essd-8-191-2016>, 2016.



- 520 Frenger, I., Münnich, M., Gruber, N., and Knutti, R.: Southern Ocean eddy phenomenology, *Journal of Geophysical Research: Oceans*, 120, 7413–7449, <https://doi.org/10.1002/2015JC011047>, _eprint: <https://onlinelibrary.wiley.com/doi/pdf/10.1002/2015JC011047>, 2015.
- Frölicher, T. L., Sarmiento, J. L., Paynter, D. J., Dunne, J. P., Krasting, J. P., and Winton, M.: Dominance of the Southern Ocean in Anthropogenic Carbon and Heat Uptake in CMIP5 Models, *Journal of Climate*, 28, 862–886, <https://doi.org/10.1175/JCLI-D-14-00117.1>, 2015.
- 525 Garcia, H., Locarnini, R., Boyer, T., Antonov, J., Mishonov, A., Baranova, O., Zweng, M., Reagan, J., and Johnson, D.: *World Ocean Atlas 2009, Volume 3: Dissolved Oxygen, Apparent Oxygen Utilization, and Oxygen Saturation*, 2013.
- Garcia, H. E., Locarnini, R. A., Boyer, T. P., Antonov, J. I., Zweng, M. M., Baranova, O. M., and Johnson, D. R.: *World Ocean Atlas 2009, Volume 4: Nutrients (Phosphate, Nitrate, and Silicate)*. S. Levitus, Ed., NOAA Atlas NESDIS 71, Tech. rep., U.S. Government Printing Office, Washington, D.C, 2010.
- 530 Gaube, P., J. McGillicuddy Jr., D., and Moulin, A. J.: Mesoscale Eddies Modulate Mixed Layer Depth Globally, *Geophysical Research Letters*, 46, 1505–1512, <https://doi.org/10.1029/2018GL080006>, 2019.
- Giddy, I., Swart, S., du Plessis, M., Thompson, A. F., and Nicholson, S.-A.: Stirring of Sea-Ice Meltwater Enhances Submesoscale Fronts in the Southern Ocean, *Journal of Geophysical Research: Oceans*, 126, e2020JC016814, <https://doi.org/10.1029/2020JC016814>, _eprint: <https://onlinelibrary.wiley.com/doi/pdf/10.1029/2020JC016814>, 2021.
- 535 Giddy, I. S., Nicholson, S.-A., Queste, B. Y., Thomalla, S., and Swart, S.: Sea-Ice Impacts Inter-Annual Variability of Phytoplankton Bloom Characteristics and Carbon Export in the Weddell Sea, *Geophysical Research Letters*, 50, e2023GL103695, <https://doi.org/10.1029/2023GL103695>, _eprint: <https://onlinelibrary.wiley.com/doi/pdf/10.1029/2023GL103695>, 2023.
- Gray, A. R., Johnson, K. S., Bushinsky, S. M., Riser, S. C., Russell, J. L., Talley, L. D., Wanninkhof, R., Williams, N. L., and Sarmiento, J. L.: Autonomous Biogeochemical Floats Detect Significant Carbon Dioxide Outgassing in the
- 540 High-Latitude Southern Ocean, *Geophysical Research Letters*, 45, 9049–9057, <https://doi.org/10.1029/2018GL078013>, _eprint: <https://onlinelibrary.wiley.com/doi/pdf/10.1029/2018GL078013>, 2018.
- Gregor, L., Lebehot, A. D., Kok, S., and Scheel Monteiro, P. M.: A Comparative Assessment of the Uncertainties of Global Surface Ocean CO₂ Estimates Using a Machine-Learning Ensemble (CSIR-ML6 Version 2019a) – Have We Hit the Wall?, *Geoscientific Model Development*, 12, 5113–5136, <https://doi.org/10.5194/gmd-12-5113-2019>, 2019.
- 545 Gruber, N., Landschützer, P., and Lovenduski, N. S.: The variable Southern Ocean carbon sink, *Annual review of marine science*, 11, 159–186, 2019.
- Gruber, N., Bakker, D. C. E., DeVries, T., Gregor, L., Hauck, J., Landschützer, P., McKinley, G. A., and Müller, J. D.: Trends and Variability in the Ocean Carbon Sink, *Nature Reviews Earth & Environment*, 4, 119–134, <https://doi.org/10.1038/s43017-022-00381-x>, 2023.
- Gurvan, M., Bourdallé-Badie, R., Bouttier, P.-A., Bricaud, C., Bruciaferri, D., Calvert, D., Chanut, J., Clementi, E., Coward, A., Delrosso,
- 550 D., Ethé, C., Flavoni, S., Graham, T., Harle, J., Iovino, D., Lea, D., Lévy, C., Lovato, T., Martin, N., Masson, S., Mocavero, S., Paul, J., Rousset, C., Storkey, D., Storto, A., and Vancoppenolle, M.: NEMO ocean engine, <https://doi.org/10.5281/zenodo.1475234>, tex.version: v3.4-patch, 2019.
- Haarsma, R. J., Roberts, M. J., Vidale, P. L., Senior, C. A., Bellucci, A., Bao, Q., Chang, P., Corti, S., Fučkar, N. S., Guemas, V., von Hardenberg, J., Hazeleger, W., Kodama, C., Koenigk, T., Leung, L. R., Lu, J., Luo, J.-J., Mao, J., Mizielinski, M. S., Mizuta, R., Nobre, P.,
- 555 Satoh, M., Scoccimarro, E., Semmler, T., Small, J., and von Storch, J.-S.: High Resolution Model Intercomparison Project (HighResMIP v1.0) for CMIP6, *Geoscientific Model Development*, 9, 4185–4208, <https://doi.org/10.5194/gmd-9-4185-2016>, 2016.



- Hague, M. and Vichi, M.: A Link Between CMIP5 Phytoplankton Phenology and Sea Ice in the Atlantic Southern Ocean, *Geophysical Research Letters*, 45, 6566–6575, <https://doi.org/10.1029/2018GL078061>, 2018.
- 560 Hauck, J., Gregor, L., Nissen, C., Patara, L., Hague, M., Mongwe, P., Bushinsky, S., Doney, S. C., Gruber, N., Le Quéré, C., Manizza, M., Mazloff, M., Monteiro, P. M. S., and Terhaar, J.: The Southern Ocean Carbon Cycle 1985–2018: Mean, Seasonal Cycle, Trends, and Storage, *Global Biogeochemical Cycles*, 37, e2023GB007848, <https://doi.org/10.1029/2023GB007848>, <https://onlinelibrary.wiley.com/doi/pdf/10.1029/2023GB007848>, 2023.
- Hewitt, H. T., Roberts, M., Mathiot, P., Biastoch, A., Blockley, E., Chassignet, E. P., Fox-Kemper, B., Hyder, P., Marshall, D. P., Popova, E., Treguier, A.-M., Zanna, L., Yool, A., Yu, Y., Beadling, R., Bell, M., Kuhlbrodt, T., Arsouze, T., Bellucci, A., Castruccio, F., Gan, B., Putrasahan, D., Roberts, C. D., Van Roekel, L., and Zhang, Q.: Resolving and Parameterising the Ocean Mesoscale in Earth System Models, *Current Climate Change Reports*, 6, 137–152, <https://doi.org/10.1007/s40641-020-00164-w>, 2020.
- 565 Holte, J., Talley, L. D., Gilson, J., and Roemmich, D.: An Argo Mixed Layer Climatology and Database, *Geophysical Research Letters*, 44, 5618–5626, <https://doi.org/10.1002/2017GL073426>, 2017.
- Kessler, A. and Tjiputra, J.: The Southern Ocean as a Constraint to Reduce Uncertainty in Future Ocean Carbon Sinks, *Earth System Dynamics*, 7, 295–312, <https://doi.org/10.5194/esd-7-295-2016>, 2016.
- 570 Key, R. M., Kozyr, A., Sabine, C. L., Lee, K., Wanninkhof, R., Bullister, J. L., Feely, R. A., Millero, F. J., Mordy, C., and Peng, T.-H.: A Global Ocean Carbon Climatology: Results from Global Data Analysis Project (GLODAP): GLOBAL OCEAN CARBON CLIMATOLOGY, *Global Biogeochemical Cycles*, 18, n/a–n/a, <https://doi.org/10.1029/2004GB002247>, 2004.
- Landschützer, P., Gruber, N., Bakker, D. C. E., Stemmler, I., and Six, K. D.: Strengthening seasonal marine CO₂ variations due to increasing atmospheric CO₂, *Nature Climate Change*, 8, 146–150, <https://doi.org/10.1038/s41558-017-0057-x>, number: 2 Publisher: Nature Publishing Group, 2018.
- 575 Lauvset, S. K., Key, R. M., Olsen, A., van Heuven, S., Velo, A., Lin, X., Schirnick, C., Kozyr, A., Tanhua, T., Hoppema, M., Jutterström, S., Steinfeldt, R., Jeansson, E., Ishii, M., Perez, F. F., Suzuki, T., and Watelet, S.: A New Global Interior Ocean Mapped Climatology: The 1° × 1° GLODAP Version 2, *Earth System Science Data*, 8, 325–340, <https://doi.org/10.5194/essd-8-325-2016>, 2016.
- 580 Lecointre, A., Molines, J.-M., and Barnier, B.: Definition of the Interannual Experiment ORCA12.L46-MAL95, 1989–2007, 2011.
- Leggett, R. W. and Williams, L. R.: A Reliability Index for Models, *Ecological Modelling*, 13, 303–312, [https://doi.org/10.1016/0304-3800\(81\)90034-X](https://doi.org/10.1016/0304-3800(81)90034-X), 1981.
- Lenton, A., Tilbrook, B., Law, R. M., Bakker, D., Doney, S. C., Gruber, N., Ishii, M., Hoppema, M., Lovenduski, N. S., Matear, R. J., McNeil, B. I., Metzl, N., Mikaloff Fletcher, S. E., Monteiro, P. M. S., Rödenbeck, C., Sweeney, C., and Takahashi, T.: Sea–Air CO₂ Fluxes in the Southern Ocean for the Period 1990–2009, *Biogeosciences*, 10, 4037–4054, <https://doi.org/10.5194/bg-10-4037-2013>, 2013.
- 585 Lévy, M., Mémerly, L., and Madec, G.: The onset of a bloom after deep winter convection in the northwestern Mediterranean sea: mesoscale process study with a primitive equation model, *Journal of Marine Systems*, 16, 7–21, [https://doi.org/10.1016/S0924-7963\(97\)00097-3](https://doi.org/10.1016/S0924-7963(97)00097-3), 1998.
- Lévy, M., Mémerly, L., and Madec, G.: The onset of the Spring Bloom in the MEDOC area: mesoscale spatial variability, *Deep Sea Research Part I: Oceanographic Research Papers*, 46, 1137–1160, [https://doi.org/10.1016/S0967-0637\(98\)00105-8](https://doi.org/10.1016/S0967-0637(98)00105-8), 1999.
- 590 Lévy, M., Klein, P., Tréguier, A.-M., Iovino, D., Madec, G., Masson, S., and Takahashi, K.: Modifications of Gyre Circulation by Sub-Mesoscale Physics, *Ocean Modelling*, 34, 1–15, <https://doi.org/10.1016/j.ocemod.2010.04.001>, 2010.



- Locarnini, R. A., Mishonov, A. V., Antonov, J. I., Boyer, T. P., Garcia, H. E., Baranova, O. M., Zweng, M. M., and Johnson, D. R.: World Ocean Atlas 2009, Volume 1: Temperature. S. Levitus, Ed., NOAA Atlas NESDIS 68, Tech. Rep. NOAA Atlas NESDIS 68, U.S. Government Printing Office, Washington, D.C., 2010.
- 595 Mackay, N. and Watson, A.: Winter Air-Sea CO₂ Fluxes Constructed From Summer Observations of the Polar Southern Ocean Suggest Weak Outgassing, *Journal of Geophysical Research: Oceans*, 126, e2020JC016600, <https://doi.org/10.1029/2020JC016600>, <https://onlinelibrary.wiley.com/doi/pdf/10.1029/2020JC016600>, 2021.
- Mahadevan, A., D'Asaro, E., Lee, C., and Perry, M. J.: Eddy-Driven Stratification Initiates North Atlantic Spring Phytoplankton Blooms, *Science*, 337, 54–58, <https://doi.org/10.1126/science.1218740>, publisher: American Association for the Advancement of Science, 2012.
- 600 Marshall, J., Jones, H., Karsten, R., and Wardle, R.: Can Eddies Set Ocean Stratification?, *Journal of Physical Oceanography*, 32, 26–38, [https://doi.org/10.1175/1520-0485\(2002\)032<0026:CESOS>2.0.CO;2](https://doi.org/10.1175/1520-0485(2002)032<0026:CESOS>2.0.CO;2), publisher: American Meteorological Society Section: Journal of Physical Oceanography, 2002.
- Meier, W. N., Fetterer, F., Savoie, M., Mallory, S., Duerr, R., and Stroeve, J.: NOAA/NSIDC Climate Data Record of Passive Microwave Sea Ice Concentration, Version 3, <https://doi.org/10.7265/N59P2ZTG>, 2017.
- 605 Meijers, A. J. S.: The Southern Ocean in the Coupled Model Intercomparison Project Phase 5, *Philosophical Transactions of the Royal Society A: Mathematical, Physical and Engineering Sciences*, 372, 20130296, <https://doi.org/10.1098/rsta.2013.0296>, 2014.
- Meredith, M. P., Schofield, O., Newman, L., Urban, E., and Sparrow, M.: The Vision for a Southern Ocean Observing System, *Current Opinion in Environmental Sustainability*, 5, 306–313, <https://doi.org/10.1016/j.cosust.2013.03.002>, 2013.
- 610 Mongwe, N. P., Chang, N., and Monteiro, P. M. S.: The Seasonal Cycle as a Mode to Diagnose Biases in Modelled CO₂ Fluxes in the Southern Ocean, *Ocean Modelling*, 106, 90–103, <https://doi.org/10.1016/j.ocemod.2016.09.006>, 2016.
- Mongwe, N. P., Vichi, M., and Monteiro, P. M. S.: The Seasonal Cycle of *p*CO₂ and CO₂ Fluxes in the Southern Ocean: Diagnosing Anomalies in CMIP5 Earth System Models, *Biogeosciences*, 15, 2851–2872, <https://doi.org/10.5194/bg-15-2851-2018>, 2018.
- Monteiro, P. M. S., Gregor, L., Lévy, M., Maenner, S., Sabine, C. L., and Swart, S.: Intraseasonal variability linked to sampling alias in air-sea CO₂ fluxes in the Southern Ocean, *Geophysical Research Letters*, 42, 8507–8514, <https://doi.org/10.1002/2015GL066009>, <https://onlinelibrary.wiley.com/doi/pdf/10.1002/2015GL066009>, 2015.
- 615 Munday, D. R., Johnson, H. L., and Marshall, D. P.: Impacts and Effects of Mesoscale Ocean Eddies on Ocean Carbon Storage and Atmospheric *p*CO₂, *Global Biogeochemical Cycles*, 28, 877–896, <https://doi.org/10.1002/2014GB004836>, 2014.
- Munday, D. R., Zhai, X., Harle, J., Coward, A. C., and Nurser, A. J. G.: Relative vs. Absolute Wind Stress in a Circumpolar Model of the Southern Ocean, *Ocean Modelling*, 168, 101891, <https://doi.org/10.1016/j.ocemod.2021.101891>, 2021.
- 620 Nicholson, S.-A., Lévy, M., Jouanno, J., Capet, X., Swart, S., and Monteiro, P. M. S.: Iron Supply Pathways Between the Surface and Subsurface Waters of the Southern Ocean: From Winter Entrainment to Summer Storms, *Geophysical Research Letters*, 46, 14567–14575, <https://doi.org/10.1029/2019GL084657>, 2019.
- Olsen, A., Key, R. M., van Heuven, S., Lauvset, S. K., Velo, A., Lin, X., Schirnack, C., Kozyr, A., Tanhua, T., Hoppema, M., Jutterström, S., Steinfeldt, R., Jeansson, E., Ishii, M., Pérez, F. F., and Suzuki, T.: The Global Ocean Data Analysis Project Version 2 (GLODAPv2) – an Internally Consistent Data Product for the World Ocean, *Earth System Science Data*, 8, 297–323, <https://doi.org/10.5194/essd-8-297-2016>, 2016.
- 625 Orsi, A. H., Whitworth, T., and Nowlin, W. D.: On the Meridional Extent and Fronts of the Antarctic Circumpolar Current, *Deep Sea Research Part I: Oceanographic Research Papers*, 42, 641–673, [https://doi.org/10.1016/0967-0637\(95\)00021-W](https://doi.org/10.1016/0967-0637(95)00021-W), 1995.



- 630 Patara, L., Böning, C. W., and Biastoch, A.: Variability and Trends in Southern Ocean Eddy Activity in 1/12° Ocean Model Simulations: Changes in Southern Ocean Eddy Activity, *Geophysical Research Letters*, 43, 4517–4523, <https://doi.org/10.1002/2016GL069026>, 2016.
- Peng, G., Meier, W. N., Scott, D. J., and Savoie, M. H.: A Long-Term and Reproducible Passive Microwave Sea Ice Concentration Data Record for Climate Studies and Monitoring, *Earth System Science Data*, 5, 311–318, <https://doi.org/10.5194/essd-5-311-2013>, 2013.
- Renault, L., Molemaker, M. J., McWilliams, J. C., Shchepetkin, A. F., Lemarié, F., Chelton, D., Illig, S., and Hall, A.: Modu-
635 lation of Wind Work by Oceanic Current Interaction with the Atmosphere, *Journal of Physical Oceanography*, 46, 1685–1704, <https://doi.org/10.1175/JPO-D-15-0232.1>, 2016.
- Rieck, J. K., Böning, C. W., Greatbatch, R. J., and Scheinert, M.: Seasonal Variability of Eddy Kinetic Energy in a Global High-Resolution Ocean Model: ANNUAL CYCLE OF EDDY KINETIC ENERGY, *Geophysical Research Letters*, 42, 9379–9386, <https://doi.org/10.1002/2015GL066152>, 2015.
- 640 Rintoul, S. R.: The Global Influence of Localized Dynamics in the Southern Ocean, *Nature*, 558, 209–218, <https://doi.org/10.1038/s41586-018-0182-3>, 2018.
- Rodgers, K. B., Schwinger, J., Fassbender, A. J., Landschützer, P., Yamaguchi, R., Frenzel, H., Stein, K., Müller, J. D., Goris, N., Sharma, S., et al.: Seasonal variability of the surface ocean carbon cycle: A synthesis, *Global Biogeochemical Cycles*, 37, e2023GB007798, 2023.
- Rohr, T., Harrison, C., Long, M. C., Gaube, P., and Doney, S. C.: Eddy-Modified Iron, Light, and Phytoplankton Cell Division Rates in the
645 Simulated Southern Ocean, *Global Biogeochemical Cycles*, 34, e2019GB006380, <https://doi.org/10.1029/2019GB006380>, 2020.
- Rosso, I., Mazloff, M. R., Talley, L. D., Purkey, S. G., Freeman, N. M., and Maze, G.: Water Mass and Biogeochemical Variability in the Kerguelen Sector of the Southern Ocean: A Machine Learning Approach for a Mixing Hot Spot, *Journal of Geophysical Research: Oceans*, 125, e2019JC015877, <https://doi.org/10.1029/2019JC015877>, 2020.
- Russell, J. L., Kamenkovich, I., Bitz, C., Ferrari, R., Gille, S. T., Goodman, P. J., Hallberg, R., Johnson, K., Khazmutdinova, K., Mari-
650 nov, I., Mazloff, M., Riser, S., Sarmiento, J. L., Speer, K., Talley, L. D., and Wanninkhof, R.: Metrics for the Evaluation of the Southern Ocean in Coupled Climate Models and Earth System Models, *Journal of Geophysical Research: Oceans*, 123, 3120–3143, <https://doi.org/10.1002/2017JC013461>, 2018.
- Rustogi, P., Landschützer, P., Brune, S., and Baehr, J.: The impact of seasonality on the annual air-sea carbon flux and its interannual variability, *npj Climate and Atmospheric Science*, 6, 66, 2023.
- 655 Ryan-Keogh, T. J., Thomalla, S. J., Chang, N., and Moalusi, T.: A new global oceanic multi-model net primary productivity data product, *Earth System Science Data*, 15, 4829–4848, 2023.
- Sallée, J.-B., Shuckburgh, E., Bruneau, N., Meijers, A. J. S., Bracegirdle, T. J., Wang, Z., and Roy, T.: Assessment of Southern Ocean water mass circulation and characteristics in CMIP5 models: Historical bias and forcing response, *Journal of Geophysical Research: Oceans*, 118, 1830–1844, <https://doi.org/10.1002/jgrc.20135>, [_eprint: https://onlinelibrary.wiley.com/doi/pdf/10.1002/jgrc.20135](https://onlinelibrary.wiley.com/doi/pdf/10.1002/jgrc.20135), 2013.
- 660 Sathyendranath, S., Brewin, R. J. W., Brockmann, C., Brotas, V., Calton, B., Chuprin, A., Cipollini, P., Couto, A. B., Dingle, J., Doerffer, R., Donlon, C., Dowell, M., Farman, A., Grant, M., Groom, S., Horseman, A., Jackson, T., Krasemann, H., Lavender, S., Martinez-Vicente, V., Mazeran, C., Mélin, F., Moore, T. S., Müller, D., Regner, P., Roy, S., Steele, C. J., Steinmetz, F., Swinton, J., Taberner, M., Thompson, A., Valente, A., Zühlke, M., Brando, V. E., Feng, H., Feldman, G., Franz, B. A., Frouin, R., Gould, R. W., Hooker, S. B., Kahru, M., Kratzer, S., Mitchell, B. G., Muller-Karger, F. E., Sosik, H. M., Voss, K. J., Werdell, J., and Platt, T.: An Ocean-Colour Time Series for Use in Climate
665 Studies: The Experience of the Ocean-Colour Climate Change Initiative (OC-CCI), *Sensors*, 19, 4285, <https://doi.org/10.3390/s19194285>, 2019.



- Séférian, R., Bopp, L., Gehlen, M., Orr, J. C., Ethé, C., Cadule, P., Aumont, O., Salas y Méliá, D., Voldoire, A., and Madec, G.: Skill Assessment of Three Earth System Models with Common Marine Biogeochemistry, *Climate Dynamics*, 40, 2549–2573, <https://doi.org/10.1007/s00382-012-1362-8>, 2013.
- 670 Shao, A. E., Gille, S. T., Mecking, S., and Thompson, L.: Properties of the Subantarctic Front and Polar Front from the Skewness of Sea Level Anomaly: PROPERTIES OF THE SAF AND PF, *Journal of Geophysical Research: Oceans*, 120, 5179–5193, <https://doi.org/10.1002/2015JC010723>, 2015.
- Smith, T., Nicholson, S., Engelbrecht, F., Chang, N., Mongwe, N., and Monteiro, P.: The Heat and Carbon Characteristics of Modeled Mesoscale Eddies in the South–East Atlantic Ocean, *Journal of Geophysical Research: Oceans*, 128, <https://doi.org/10.1029/2023JC020337>, 2023.
- 675 Song, H., Long, M. C., Gaube, P., Frenger, I., Marshall, J., and McGillicuddy Jr., D. J.: Seasonal Variation in the Correlation Between Anomalies of Sea Level and Chlorophyll in the Antarctic Circumpolar Current, *Geophysical Research Letters*, 45, 5011–5019, <https://doi.org/10.1029/2017GL076246>, 2018.
- Swart, S., Chang, N., Fauchereau, N., Joubert, W., Lucas, M., Mtshali, T., Roychoudhury, A., Tagliabue, A., Thomalla, S., and Waldron, H.: Southern Ocean Seasonal Cycle Experiment 2012: Seasonal Scale Climate and Carbon Cycle Links, *South African Journal of Science*, 108, 11–13, 2012.
- 680 Tagliabue, A., Mtshali, T., Aumont, O., Bowie, A. R., Klunder, M. B., Roychoudhury, A. N., and Swart, S.: A Global Compilation of Dissolved Iron Measurements: Focus on Distributions and Processes in the Southern Ocean, *Biogeosciences*, 9, 2333–2349, <https://doi.org/10.5194/bg-9-2333-2012>, 2012.
- 685 Tagliabue, A., Sallée, J.-B., Bowie, A. R., Lévy, M., Swart, S., and Boyd, P. W.: Surface-water iron supplies in the Southern Ocean sustained by deep winter mixing, *Nature Geoscience*, 7, 314–320, <https://doi.org/10.1038/ngeo2101>, number: 4 Publisher: Nature Publishing Group, 2014.
- Tagliabue, A., Aumont, O., DeAth, R., Dunne, J. P., Dutkiewicz, S., Galbraith, E., Misumi, K., Moore, J. K., Ridgwell, A., Sherman, E., Stock, C., Vichi, M., Völker, C., and Yool, A.: How Well Do Global Ocean Biogeochemistry Models Simulate Dissolved Iron Distributions?, *Global Biogeochemical Cycles*, 30, 149–174, <https://doi.org/10.1002/2015GB005289>, 2016.
- 690 Thomalla, S. J., Fauchereau, N., Swart, S., and Monteiro, P. M. S.: Regional Scale Characteristics of the Seasonal Cycle of Chlorophyll in the Southern Ocean, *Biogeosciences*, 8, 2849–2866, <https://doi.org/10.5194/bg-8-2849-2011>, 2011.
- Thomalla, S. J., Nicholson, S.-A., Ryan-Keogh, T. J., and Smith, M. E.: Widespread changes in Southern Ocean phytoplankton blooms linked to climate drivers, *Nature Climate Change*, 13, 975–984, <https://doi.org/10.1038/s41558-023-01768-4>, number: 9 Publisher: Nature Publishing Group, 2023.
- 695 Treguier, A. M., de Boyer Montégut, C., Bozec, A., Chassignet, E. P., Fox-Kemper, B., McC. Hogg, A., Iovino, D., Kiss, A. E., Le Sommer, J., Li, Y., Lin, P., Lique, C., Liu, H., Serazin, G., Sidorenko, D., Wang, Q., Xu, X., and Yeager, S.: The mixed-layer depth in the Ocean Model Intercomparison Project (OMIP): impact of resolving mesoscale eddies, *Geoscientific Model Development*, 16, 3849–3872, <https://doi.org/10.5194/gmd-16-3849-2023>, publisher: Copernicus GmbH, 2023.
- 700 Uchida, T., Balwada, D., Abernathy, R., McKinley, G., Smith, S., and Lévy, M.: The Contribution of Submesoscale over Mesoscale Eddy Iron Transport in the Open Southern Ocean, *Journal of Advances in Modeling Earth Systems*, 11, 3934–3958, <https://doi.org/10.1029/2019MS001805>, 2019.
- Uchida, T., Balwada, D., P. Abernathy, R., A. McKinley, G., K. Smith, S., and Lévy, M.: Vertical Eddy Iron Fluxes Support Primary Production in the Open Southern Ocean, *Nature Communications*, 11, 1125, <https://doi.org/10.1038/s41467-020-14955-0>, 2020.



- 705 Verdy, A. and Mazloff, M. R.: A Data Assimilating Model for Estimating Southern Ocean Biogeochemistry, *Journal of Geophysical Research: Oceans*, 122, 6968–6988, <https://doi.org/10.1002/2016JC012650>, 2017.
- Wang, J., Mazloff, M. R., and Gille, S. T.: The Effect of the Kerguelen Plateau on the Ocean Circulation, *Journal of Physical Oceanography*, 46, 3385–3396, <https://doi.org/10.1175/JPO-D-15-0216.1>, 2016.
- Whitt, D. B., Lévy, M., and Taylor, J. R.: Submesoscales Enhance Storm-Driven Vertical Mixing of Nutrients: Insights From a Biogeo-
710 chemical Large Eddy Simulation, *Journal of Geophysical Research: Oceans*, 124, 8140–8165, <https://doi.org/10.1029/2019JC015370>, 2019.
- Whitworth, T. and Peterson, R. G.: Volume Transport of the Antarctic Circumpolar Current from Bottom Pressure Measurements, *Journal of Physical Oceanography*, 15, 810–816, [https://doi.org/10.1175/1520-0485\(1985\)015<0810:VTOTAC>2.0.CO;2](https://doi.org/10.1175/1520-0485(1985)015<0810:VTOTAC>2.0.CO;2), 1985.
- Williams, N. L., Juranek, L. W., Feely, R. A., Russell, J. L., Johnson, K. S., and Hales, B.: Assessment of the Carbonate Chemistry Seasonal
715 Cycles in the Southern Ocean From Persistent Observational Platforms, *Journal of Geophysical Research: Oceans*, 123, 4833–4852, <https://doi.org/10.1029/2017JC012917>, 2018.